Title: Non-redundant cardiolipin synthases shape membrane composition and support stress resilience in *Bacteroides fragilis*

Authors: Matthew K. Schnizlein[1], Bong Jin Hong[1,2], Jennifer N.T. Nguyen[3], Katarina Jones[4,5], Alyssa I. Rodriguez[3], Aretha Fiebig[1,6], Shawn R. Campagna[4,5], Marcy J. Balunas[3,7], Thomas V. O'Halloran[1,2,8], Sean Crosson[1,6,*]

*corresponding author: crosson4@msu.edu

Affiliations

[1]Department of Microbiology, Genetics & Immunology, Michigan State University, East Lansing, MI, USA

[2]Elemental Health Institute, Michigan State University, East Lansing, MI, USA

[3]Department of Medicinal Chemistry, University of Michigan, Ann Arbor, MI, USA

[4]Biological and Small Molecule Mass Spectrometry Core, University of Tennessee-Knoxville, TN, USA

[5]Department of Chemistry, University of Tennessee-Knoxville, TN, USA

[6]BioMolecular Science Gateway, Michigan State University, East Lansing, MI, USA

[7]Department of Microbiology and Immunology, University of Michigan, Ann Arbor, MI, USA

[8]Department of Chemistry, Michigan State University, East Lansing, MI, USA

Abstract: *Bacteroides fragilis* is an anaerobic resident of the human gut known to tolerate the toxic effects of host-produced and microbially-modified bile acids. Two conserved genes, *clsA* and *clsB*, encode putative cardiolipin synthases that have been linked to bile acid tolerance, but their physiological roles remain undefined. Phylogenetic analysis indicates that *Bacteroides* spp. ClsA

and ClsB diverge from the well-characterized cardiolipin synthases of Gammaproteobacteria and Firmicutes. Here, we show that these enzymes have distinct cardiolipin synthase activities and make non-redundant contributions to *B. fragilis* fitness under gut-relevant stress conditions, including osmotic stress, disruption of membrane potential, and exposure to the bile acid deoxycholate. Although deoxycholate treatment perturbed K^+/Na^+ homeostasis in *B. fragilis*, deletion of *clsA* or *clsB* did not significantly alter intracellular ion levels, suggesting that cardiolipin loss does not substantially impact ion balance under standard cultivation conditions. High-resolution lipidomic analyses showed that cardiolipin comprises less than 1% of *B. fragilis* membranes and that ClsA and ClsB produce distinct cardiolipin products with unique acyl chain lengths and levels of unsaturation. Deletion of either *cls* gene led to Cls-specific remodeling of *B. fragilis* envelope lipid content, which was also associated with shifts in non-lipid metabolites indicative of stress-induced metabolic changes. These results define distinct roles for ClsA and ClsB in shaping *B. fragilis* membrane composition, metabolism, and stress resilience, and highlight cardiolipin as a key determinant of fitness under bile acid stress.

Importance: Inflammatory bowel diseases are a growing global health concern, motivating efforts to understand how inflammation-associated microbes, such as *B. fragilis*, adapt to and persist in stress conditions typical of the intestinal environment. Our targeted genetic analyses reveal that the cardiolipin synthases ClsA and ClsB make non-redundant contributions to *B. fragilis* fitness under bile acid exposure and other gut-relevant stress conditions. Complementary omics-based approaches show that these enzymes produce chemically distinct cardiolipin species and that their loss leads to specific remodeling of membrane lipid composition and cellular metabolite profiles. Together, our results indicate that cardiolipin synthases contribute to membrane and metabolic adaptation in *B. fragilis*, supporting stress resilience in the presence of bile acids and other gut-relevant stressors.

53 **INTRODUCTION**

54 To successfully occupy gut niches and maintain homeostasis, bacteria must preserve
55 membrane integrity to resist phage attack, host immune pressures, and membrane-disrupting
56 molecules such as bile acids (1-7). The functional properties of membranes are shaped by the
57 diverse lipids classes of which they are made, each characterized by an array of structural species
58 (8-10). For example, bacteria can alter their membrane fluidity and/or permeability by modulating
59 the length of phospholipid acyl tails in response to extracellular conditions (8, 11). Bacteria also
60 adjust the abundance of different phospholipid types or modify lipid headgroups through reactions
61 such as aminoacylation (12-16).

62 In addition to protecting against external threats, membranes also help support cellular
63 metabolism by maintaining a potential energy source in the form of ion gradients, such as
64 hydrogen (protons, H^+), sodium (Na^+), and potassium (K^+) (17). One of the best-known functions
65 of proton gradients is to power rotary ATPase complexes (i.e., F_oF_1) associated with aerobic and
66 anaerobic respiration (18-22). Prokaryotes as well as eukaryotes maintain Na^+ and K^+ at
67 intracellular concentrations that are lower and higher, respectively, relative to their environment,
68 which drives the transport of metals or other molecules across the membrane (23, 24).

69 Cardiolipins, which make up 1–5% of the bacterial membrane, play an integral role in
70 maintaining ion gradients (25-30). This class of membrane lipid comprises two covalently bonded
71 phospholipids, such as phosphatidylglycerol (PG) or in some cases phosphatidylethanolamine
72 (PE) (31). While cardiolipins increase proton permeability across model liposome membranes
73 (28, 32), they also contribute to membrane stabilization by enhancing hydrogen bonding, reducing
74 water permeability and sustaining membrane potential during stress-induced membrane
75 depolarization (32, 33). In addition, several protein complexes require cardiolipin for proper
76 function, including some two-component systems, protein translocation machinery, and
77 respiratory complexes (34-39).

78 *Escherichia coli* has three well-studied genes responsible for cardiolipin biosynthesis:
79 *clsA*, *clsB* and *clsC* (31, 40). Each gene makes distinct contributions to *E. coli* physiology
80 depending on growth phase, with *clsA* being the primary *cls* used during logarithmic (log)-phase
81 growth and all three used during stationary phase (26, 31). While ClsA and ClsB act on PG as the
82 sole substrate, ClsC synthesizes cardiolipin from PE as well as PG (31, 41-43). The Cls enzymes
83 encoded by these genes are thought to synthesize three structural families of cardiolipin, which
84 have four (cardiolipin), three (monolysocardiolipin) and two acyl tails (dilysocardiolipin),
85 respectively (for chemical structures, see Fig. 6A) (44). However, mechanistic insight into bacterial
86 cardiolipin biosynthesis and function largely comes from studies in *E. coli* and other
87 Enterobacteriaceae. Expanding this research across diverse bacterial lineages is essential for
88 uncovering the broader physiological roles of this important lipid class.

89 The gut microbe *Bacteroides fragilis* is a gram-negative facultative anaerobe that must
90 maintain membrane integrity for gut fitness (45-47). While *B. fragilis* strains, particularly those that
91 carry the fragilysin toxin, are linked to colorectal cancer and other diseases (48), it constitutes
92 about 1–5% of the microbiota in otherwise healthy humans (49, 50). We recently identified two
93 cardiolipin synthases as critical for the survival of the non-toxigenic *B. fragilis* strain P207 in the
94 presence of physiologically relevant levels of deoxycholate, a secondary bile acid (51). *B. fragilis*
95 P207 was isolated from the ileoanal pouch of a patient with ulcerative colitis (UC) and is
96 representative of *B. fragilis* populations that can dominate prior to the onset of pouchitis (52), a
97 condition characterized by UC-like inflammation of the ileoanal pouch following colectomy (53).
98 In this study, we build on our previous findings by investigating the roles of the two *B. fragilis*
99 cardiolipin synthases across a broader range of membrane stress conditions. Since cardiolipin
100 synthases are largely uncharacterized in the Bacteroidota, our work provides foundational
101 knowledge about this important class of enzymes in a dominant group of gut microbes (54). Using
102 a combination of approaches, we demonstrate that the two *cls* genes in *B. fragilis* P207, *clsA* and
103 *clsB*, are evolutionarily and functionally distinct from *cls* homologs in *E. coli* and other well-studied

104 bacterial phyla. These genes encode non-redundant enzymes that contribute structurally unique
105 cardiolipin species to the membrane, conferring distinct physiological advantages under stress.
106 We further show that *clsA* and *clsB* differ in their expression profiles and that mutants lacking
107 each gene produce distinct cardiolipin species as well as distinct metabolomic profiles, supporting
108 complementary roles in maintaining membrane homeostasis and adapting to diverse
109 environmental conditions.
110

111 **RESULTS**

112 **B. fragilis *P207 ClsA and ClsB are cardiolipin synthases***

113 The two *B. fragilis* P207 genes, ptos_000612 (*clsA*) and ptos_003252 (*clsB*), encode
114 proteins with predicted cardiolipin synthase domains (TIGR04265, PFAM13091, cd09112),
115 though *clsA* and *clsB* have low nucleotide (52.4%) and amino acid sequence (29.6%) identity to
116 each other (Fig. 1A). The low primary structure identity (≤30%) of ClsA and ClsB to *E. coli* Cls
117 proteins limited our ability to predict their specific enzymatic activities based on sequence alone
118 (Fig. 1A). Furthermore, *E. coli* ClsC did not align well with ClsA or ClsB from either *B. fragilis* or
119 *E. coli* (Fig. 1A, B). We therefore excluded ClsC from further comparisons.

120 ClsA and ClsB from *B. fragilis* and *E. coli* exhibit high amino acid conservation in two
121 regions around their predicted active sites but share limited identity across the remainder of the
122 protein (Fig. 1B, C). The Cls proteins from both species harbor two phospholipase-D active site
123 motifs H-X-K-X(4)-D (26, 42), indicative of phospholipase-D activity (Fig. 1D). Indeed, deleting
124 either *clsA* (Δ*clsA*) or *clsB* (Δ*clsB*) in *B. fragilis* resulted in a partial loss of cellular cardiolipin
125 accumulation relative to the wild-type (WT) strain; deleting both genes (Δ*clsA* Δ*clsB*) completely
126 abolished cardiolipin accumulation (Fig. 1E). We conclude that *clsA* and *clsB* in *B. fragilis* P207
127 encode *bona fide* cardiolipin synthases. A more comprehensive analysis of how deletion of *clsA*

128 and *clsB* affects the membrane lipid composition of the *B. fragilis* envelope is presented in
129 sections below.
130
131 ***The cardiolipin synthases* of Bacteroides *sp. occupy a distinct phylogenetic cluster among***
132 ***dominant gut bacterial phyla***
133 To evaluate the relatedness between *Bacteroides* Cls proteins and those encoded by other
134 gut microbes, we performed pairwise alignments of Cls sequences from dominant bacterial phyla
135 present in the human gut. These sequences clustered according to their evolutionary heritage,
136 except for the Bacillota, which had two clusters (Fig. 1F). Based on this result, we conclude that
137 each cardiolipin synthase originated from a proto-lineage, rather than having been horizontally
138 transferred.
139 We next evaluated Cls protein sequences within the *Bacteroides* genus. We aligned 301
140 *Bacteroides* protein sequences containing the TIGR04265 domain (i.e. cardiolipin synthases).
141 Most genomes encoded two cardiolipin synthases that partitioned into distinct clusters (Fig. S1).
142 Notably, the *B. thetaiotaomicron* genome encodes a third Cls that is distinct from the other two
143 *Bacteroides* Cls clusters (Fig S1) indicating an evolutionarily distant introduction. We designate
144 cluster 1 homologs as ClsA based on our observation that both *B. fragilis* and *E. coli* ClsA proteins
145 are predicted to have two N-terminal transmembrane helices, suggesting a similar mode of post-
146 translational processing (55, 56). We named the cluster 2 homologues ClsB, as they represent
147 proteins from the second and only other annotated *cls* gene in most *Bacteroides*. We left the third
148 *cls* gene, which we identified only in *B. thetaiotaomicron*, unnamed and did not further
149 characterize it.
150 Within the *Bacteroides* genus, the chromosomal gene neighborhoods around *clsA* (Fig.
151 S2A) and *clsB* (Fig. S2B) are highly conserved; this conservation is lost outside the *Bacteroides*.
152 Thus, the genomic context of *clsA* and *clsB* provides some indication of the identity of each *cls*
153 gene, specifically within the *Bacteroides* lineage. This evidence also supports the hypothesis that

154 taxa inherited each *cls* gene in two distinct regions of the chromosome. Considering this
155 phylogeny, our analysis of the *B. fragilis cls* genes presented below offer insight into the function
156 of the two broadly distributed cardiolipin synthases across the genus *Bacteroides*.
157

158 **clsA *and* clsB *deletion mutants have growth defects under membrane stress***

159 To explore the functions of the two cardiolipin synthases in *B. fragilis* P207, we generated
160 mutant strains harboring in-frame deletions of *clsA* (Δ*clsA*) and *clsB* (Δ*clsB*), and a strain lacking
161 both *cls* genes (Δ*clsA* Δ*clsB*). We also generated corresponding genetic complementation strains
162 bearing *clsA* or *clsB* integrated at a neutral heterologous site in the chromosome. We assessed
163 the growth characteristics of these *B. fragilis* strains under stress conditions that perturb various
164 aspects of membrane biology (Fig. 2). The treatments in this study included: 1) the detergents
165 deoxycholate and sodium dodecyl sulfate (SDS); 2) low pH; 3) the salts NaCl and KCl; and 4) the
166 ionophores monensin A (for Na^+) and nigericin (for K^+ and H^+) to disrupt transmembrane ion
167 gradients. Treatment concentrations were chosen based on their effect on WT strain growth.

168 In the absence of treatment, all strains grew equally well (Figs. 2A, S3A, B). Treatment
169 with the detergents deoxycholate (at 0.01% [w/v]; Fig. 2A, S3) or SDS (at 0.002% [w/v]) (Fig. 2B)
170 limited the growth of the *cls* mutant strains to a greater extent than WT. Deoxycholate affected
171 maximum OD_{600} in the Δ*clsA* Δ*clsB* att::*clsA* strain, and both max OD_{600} and growth rate the Δ*clsA*
172 Δ*clsB* strain. SDS treatment mainly affected lag time, decreasing the max OD_{600} values in the first
173 20 h of growth. Doubling time defects appeared as little or no growth, rather than slower growth
174 (Fig. 2B). Under both detergent conditions, the deletion of *clsB* had a larger effect on fitness than
175 deletion of *clsA* (Figs. 2A, B, S3) and deletion of both genes (Δ*clsA* Δ*clsB*) had an additive effect.
176 300 mM K^+ or Na^+ (Fig. 2C, D) also lowered the growth rate and maximum OD_{600} of the mutant
177 strains relative to WT (Fig. S3). Both Δ*clsA* and Δ*clsB* strains exhibited similar phenotypes, with
178 the Δ*clsA* Δ*clsB* strain showing more pronounced effects. Lowering the medium pH from 6.9 to

179 pH 5.5 (i.e., higher [H^+]) had a detrimental effect on all *B. fragilis* strains, with no clear *cls*-
180 dependent growth defects (Fig. 2E).

181 The ionophores nigericin and monensin A dissipate ion gradients by mediating the
182 exchange of ions across the inner membrane (57, 58). Specifically, nigericin is a potassium-
183 selective ionophore and a H^+-K^+ antiporter, erasing both gradients by acidifying the cytoplasm and
184 moving K^+ out of the cell (57). Monensin A is a sodium-selective ionophore with a 16-fold
185 preference for Na^+ over K^+, but can also affect H^+ gradients (57-59). Under either nigericin or
186 monensin A treatment, *clsB* deletion decreased strain fitness relative to the WT (Fig. 2F, G).
187 However, strains harboring *clsB* but lacking *clsA* (Δ*clsA* and Δ*clsA* Δ*clsB* att::*clsB*) exhibited a
188 higher maximum OD_{600} relative to the WT (Fig. S3).

189 We conclude that deleting *clsB* results in greater fitness defects than loss of *clsA* under
190 membrane perturbations. Furthermore, a functional ClsA limits growth under nigericin and
191 monensin A treatment, as we observed increased culture density in the Δ*clsA* strains. These
192 growth phenotypes provide evidence that ClsA and ClsB have distinct roles in *B. fragilis*
193 membrane physiology.

194

195 ***Loss of cardiolipin changes cell shape***

196 Given that in many bacteria, cardiolipin influences cell division, morphology, and
197 membrane fluidity (60-67), we asked whether loss of Cls function in *B. fragilis* would affect cell
198 shape. Deletion of either *cls* gene did not markedly affect overall rod-like cell shape or cellular
199 length distribution (Fig. S4A, B). However, cells lacking *clsA* (i.e., Δ*clsA* and Δ*clsA* Δ*clsB* strains;
200 Figs. 3A, B and S4C) were narrower. While cells lacking *clsB* were not significantly narrower than
201 WT, this cell population did have a broader cell width distribution compared to WT, suggesting a
202 role for ClsB in cell size regulation (F-test, WT to Δ*clsB* $p = 0.019$, WT to Δ*clsA* Δ*clsB att:clsA* $p <$
203 0.001, WT variances compared to Δ*clsA* and Δ*clsA* Δ*clsB* were not significantly different; Figs. 3A

204 and S4C). Both phenotypes could be genetically complemented. These results demonstrate that
205 ClsA and ClsB influence cell width in *B. fragilis* (Fig. 3A, B).
206
207 **B. fragilis *cardiolipin synthase genes have distinct expression profiles***
208 Considering the unique phenotypes of the Δ*clsA* and Δ*clsB* mutant strains, we
209 hypothesized that these genes have distinct expression patterns. To test this idea, we quantified
210 *clsA* and *clsB* transcripts levels across growth phases and stress conditions. *clsB* transcript levels
211 were four-fold higher during logarithmic (log) phase growth than in stationary phase, while *clsA*
212 expression was two-fold higher in stationary phase (Fig. 4A). During logarithmic growth, deletion
213 of either *cls* gene did not affect the transcript levels of the other (Fig. 4B). However, in stationary
214 phase, the deletion of *clsA* led to an 8-fold increase in *clsB* transcripts. No change in *clsA*
215 transcripts were observed upon *clsB* deletion (Fig. 4B). We conclude that the two cardiolipin
216 synthase genes of *B. fragilis* have distinct, growth-phase dependent expression profiles and that
217 *clsB* transcript upregulation in the Δ*clsA* strain may compensate for loss of ClsA activity.
218 To test if membrane stress influences the expression of the *cls* genes, we subjected cells
219 to acute stress for 20 minutes and harvested RNA. While SDS treatment did not affect *cls*
220 transcript levels, we observed a two-fold increase in *clsA* expression and a small decrease in *clsB*
221 transcripts after 0.01% deoxycholate and 300 mM K^+ treatments (Fig. 4C) (51). Acidic pH did not
222 alter *cls* transcript levels, but basic pH did decrease transcript levels of both genes (Fig. 4C).
223 Finally, we detected differences under ionophore treatment, although the biological significance
224 of these smaller changes is unclear (Fig. 4C).
225
226 ***Loss of cardiolipin synthase genes does not have a major impact on homeostasis of major***
227 ***cellular elements***
228 As cardiolipins play an important role in maintaining membrane barrier integrity (25-27,
229 68, 69), we used inductively coupled plasma mass spectrometry (ICP-MS) to quantitatively define

230 amounts of certain elements in *B. fragilis* cells and measure the effect of ClsA and/or ClsB or
231 stress treatment on those elements. While cell washing is routinely used to prepare samples for
232 metal analysis, it can disrupt intracellular levels of elements (Fig. S5A). Therefore, we used a
233 wash-free ICP-MS assay to minimize perturbation during sample preparation, adapted here for
234 bacterial cultures (70). Using this approach, we found that *B. fragilis* P207 cells grown in
235 supplemented brain heart infusion (BHIS) medium contained 550 mM phosphorus (P), 430 mM
236 potassium (K), 98 mM sulfur and 63 mM sodium (Na) (Fig. S5C, medium elemental concentrations
237 shown in S5B).

238 To compare strains, we normalized intracellular element levels to phosphorus content, an
239 accepted practice in this type of analysis (71). This revealed no significant differences across the
240 *ΔclsA*, *ΔclsB*, or double-deletion strains in the relative levels of elements detected (Fig. 5A, B,
241 and S5C). Notably, given the lack of strain-dependent defects in CFU viability, we observed shifts
242 in relative phosphorus content per CFU across *cls* mutants that was consistent with differences
243 in the OD_{600}/CFU ratios (Fig. S5E-G). Furthermore, sulfur levels scaled proportionally with
244 phosphorus across samples (Fig. S5D and S5G). While P and S abundance can vary across
245 physiological states of the cell, they are tightly regulated (72, 73). Together, the elemental
246 composition and OD_{600} data suggest that *cls* deletion can alter the ability of *cls* deletion strains to
247 consistently form colonies.

248 Like most organisms, *B. fragilis* maintains a higher concentration of intracellular K^+ (+400
249 ΔmM) and lower concentration of intracellular Na^+ (-67 ΔmM) than the surrounding environment
250 (Fig. 5C, D). Exposure to deoxycholate, a microbially-modified bile acid, led to decreased
251 intracellular K^+ and increased Na^+ contents, providing evidence that this treatment indeed disrupts
252 transmembrane ion gradients in *B. fragilis* (Figs. 5C, D & S5I-J). The observed increase in
253 intracellular P per CFU (Fig. S5K) suggests that some of these changes could result from the
254 presence of non-viable cells (Fig. S5L), as these cells would retain the S and P mass associated
255 with large molecules like proteins and nucleotides, while smaller, more permeable elements would

256 be lost across damaged membranes (74, 75). Treatment with the sodium selective ionophore,
257 monensin A, did not affect K^+ levels but caused a 32 mM increase in intracellular Na^+ (Fig. 5C,
258 D). By contrast, treatment with the potassium selective ionophore, nigericin, caused no detectable
259 effect on either K^+ or Na^+ content, suggesting that nigericin may require more than 20 min to act
260 on *B. fragilis*, or that the cells quickly adapt to the imposed ionic disturbance (Fig. 5C, D).
261

262 ***Membrane lipid composition of WT* B. fragilis *P207***

263 Through tandem mass spectrometric-based lipidomics (MS/MS), we characterized lipid
264 species present in *B. fragilis* P207 membranes using both negative and positive electrospray
265 ionization modes. To get an overall picture of WT cell membranes, we calculated the relative peak
266 area abundance for lipids detected in negative ionization mode. This analysis revealed that WT
267 cell membranes were predominantly composed of phospholipids (47% of total peak areas) and
268 ceramides (42%). The remaining abundance consisted of saccharolipids, diacylglycerols and *N*-
269 acyl lipids (Figs. 6A & S6A). The major phospholipids were species of PE (37% of total peak
270 areas), PS (7.2%) and PG (1.5%) (Fig. 6A, B, Table S4). Cardiolipin species accounted for
271 approximately 0.33% of membrane lipids detected (Fig. 6B, C). Dominant ceramides were
272 ceramide phosphoethanolamine (31.7% of total peak area) and ceramide beta-hydroxy fatty acid-
273 dihydrosphingosine (8.6%). These results are consistent with previous studies on *Bacteroides*
274 membrane lipid contents (76-78).

275 Since cardiolipin synthases use phospholipids as substrates, we investigated the types of
276 PA, PE, PS and PG species. For PA, PS and PE, the dominant lipid types were fully saturated
277 (30:0), comprising 85.8%, 60.7% and 57.1% of their respective classes (Fig. S6B). The most
278 prevalent PG species was 32:0 (54.5%, Fig. S6B). *B. fragilis* membranes also contained
279 lysophospholipids at lower levels than their two-acyl tailed versions (Fig. 6A), the most abundant
280 species of which were fully saturated at C_{15} chains for lysophosphatidylethanolamine (LPE;
281 76.9%) and lysophosphatidylserine (LPS; 54.9%), and unsaturated at 18:3 for lysophosphatidic

282 acid (LPA; 70.5%) (Fig. S6C). Ether-linked lipids and cardiolipin lipid pools showed much greater
283 diversity in their constituent acyl chains (Fig. S6D–F).
284
285 **ClsA *and* ClsB *mutants have distinct cardiolipins profiles***
286 We compared the membrane lipid profiles of the *B. fragilis* P207 WT strain and the derived
287 Δ*clsA*, Δ*clsB*, and Δ*clsA* Δ*clsB* mutant strains (Fig. 1E). While the overall abundance of the
288 dominant lipid classes did not vary significantly among the WT and *cls* mutant strains (Fig. 6B),
289 abundances of cardiolipin and monolysocardiolipin were lower in the *cls* deletion mutants (CL and
290 MLCL; Fig. 6C). Total cardiolipin levels were lower in the Δ*clsA*, Δ*clsB*, and Δ*clsA* Δ*clsB* strains
291 compared to WT, with the double knockout strain having no measurable cardiolipin (Fig. 6C). We
292 detect lower MLCL levels only in strains lacking *clsB*, indicating that ClsB is primarily responsible
293 for their biosynthesis (Fig. 6C). Notably, the deletion of both *clsA* and *clsB* led to no change in the
294 detected dilysocardiolipin (DLCL), indicating that in contrast to *E. coli* where Cls proteins
295 synthesize these lipids, a different enzymatic pathway is responsible for biosynthesis of DLCLs in
296 *B. fragilis* (Figs. 6C and S6H) (31, 41).
297 Principal component analysis (PCA) of membrane lipid peak areas revealed that each
298 mutant strain clustered separately, indicating that ClsA and ClsB independently shape membrane
299 lipid composition, while the double knockout reflected the combined loss of both functions (Fig.
300 6D). K-means clustering of lipid changes in *cls* deletion mutants relative to WT identified four
301 distinct lipid subpopulations (Fig. 6E). Clusters 1 and 2 were composed almost entirely of
302 cardiolipin, monolysocardiolipin and hexosylceramides (i.e., cluster 1 = AHexCer, cluster 2 =
303 AHexCer, Hex2Cer, HexCer_HDS), and were absent in the Δ*clsA* Δ*clsB* double deletion strain.
304 On average, the peak area of lipids in cluster 3 was significantly lower in strains lacking ClsA,
305 while cluster 4 lipids were significantly higher in strains lacking ClsB (Fig. 7A). Lipids from cluster
306 1 were largely missing is strains without *clsB*, and lipids from cluster 2 were largely missing in
307 strains without *clsA*. We therefore refer to these as *clsB*- and *clsA*-associated lipid clusters,

308 respectively. From these results, we conclude that ClsA and ClsB catalyze the production of
309 distinct lipid species in *B. fragilis*, consistent with the unique phenotypes observed in their
310 respective deletion mutants (Fig. 2).
311
312 ***ClsA and ClsB differentially influence cardiolipin saturation and membrane composition***
313 To better understand the roles of ClsA and ClsB in cardiolipin biosynthesis, we analyzed
314 the acyl chain length and degree of unsaturation in CL and MLCL species from lipid clusters 1
315 and 2. The cardiolipins associated with ClsA and with ClsB exhibited a different distribution of
316 chain lengths, including a subset of longer species that were only detected when ClsB was
317 present (Figs. 7B and S7A). The major differences between ClsA- and ClsB-associated lipids
318 were in acyl chain unsaturation: ClsA-associated cardiolipins were enriched in species with 3 and
319 11 double bonds, whereas ClsB-associated cardiolipins were enriched with 1, 2, and 14 double
320 bonds (Fig. 7C & S7B). These unique lipid profiles provide evidence that ClsA and ClsB have
321 distinct substrate preferences.
322 To determine whether *cls* deletions alter the membrane lipidome globally, we performed
323 PCA on the lipid profiles of each sample excluding cardiolipins. This analysis showed that each
324 strain still clustered separately with an additive phenotype, suggesting broad ranging, *cls*-specific
325 changes (Fig. S7D). Upon loss of cardiolipin biosynthesis in *B. fragilis*, we observe altered
326 membrane lipid composition, including shortening the acyl chain length of
327 phosphatidylethanolamine (PE), phosphatidylglycerol (PG) and phosphatidylserine (PS) species
328 (Figs. 7D and S7D). This shift was coupled with increases in lipid acyl chains with a high number
329 of total unsaturations (Figs. 7E and S7E). The combined effect of shorter acyl chains and
330 increased unsaturation is predicted to alter membrane fluidity and permeability, potentially
331 compensating for cardiolipin loss. Additional remodeling occurred in non-phospholipid lipid
332 classes, with lipid families such as fatty acids (FAHFA) and hexosylceramides (HexCer-HDS)
333 more affected by *clsA* deletion, while *N*-acyl lipids (NAOrn, NAE, NAGlySer), phosphoceramides

334 (CerP), other hexosylceramides (AHexCer, Hex3Cer), and ether-linked glycolipids (EtherMGDG)
335 were more affected by *clsB* deletion (Fig. 7F–H). These patterns were confirmed by elastic net
336 regression, which distinguished the double mutant from WT based reductions in Cluster 1 (CL
337 75:3, AHexCer [O-22:6]51:9:2O) and Cluster 3 (PE O-38:0:2O) lipid species, as well as increases
338 in two Cluster 4 lipids (NAGlySer 29:0:1O, PC O-24:4:1O). Together, these results provide
339 evidence that ClsA and ClsB have distinct biosynthetic activities that contribute to cardiolipin
340 diversity, and that the loss of either enzyme perturbs the membrane lipidome in unique ways.
341 These broader shifts in membrane composition upon *cls* gene deletion likely underlie the distinct
342 phenotypes observed in each mutant strain.
343
344 ***ClsA and ClsB loss lead to distinct changes in non-lipid metabolites***
345 Since we observed distinct shifts in non-cardiolipin lipids, we hypothesized that these
346 shifts might extend to other *B. fragilis* metabolites under non-stressed conditions. Using LC-
347 tandem mass spectrometry (LC-MS/MS), we found that each strain had unique metabolite
348 profiles, with Δ*clsB* being the most distinct (Figs. 8A-C). Using publicly available databases, 56%
349 of all features were annotated, with 83% of those matches from small molecule databases.
350 Approximately 27% of the metabolomic features were not shared between all the strains, with
351 ~14% of the features only depleted in Δ*clsA*, Δ*clsB*, or Δ*clsA* Δ*clsB* (Fig. 8B). Notably, we observed
352 that the effect of *clsA* and *clsB* deletion is not additive, with *clsB* deletion showing the most
353 profound alterations on the metabolomic profiles by hierarchical clustering (Fig. 8C).
354 To determine metabolites that are associated with *cls* deletions, we performed pathway
355 enrichment analysis comparing feature abundances between the WT and double knockout strain.
356 As with the lipidomics analysis above, we identified fatty amides as the most differentially enriched
357 pathway, followed by the fatty esters and sphingolipids (Fig. S8). Several non-lipid classes were
358 also identified, including alkaloids, amino acids, amino sugars, benzoic acid esters, and
359 pyrimidines as the most differentially enriched pathways with high enrichment factors and

360 significant p-values (Fig. 8D). Analysis of amino acids and related compounds identified lipid-
361 conjugated homoserine lactones (HSLs) and fatty amides to be substantially changed in the
362 mutant strains (Figs 8E–F). The lipid-conjugated HSLs, which are small signaling molecules
363 crucial in quorum sensing (79), were mainly associated with *clsB* deletion. In these mutants, levels
364 of long-chain HSLs (e.g., *N*-hexadecanoyl HSL) were reduced, while shorter lipid conjugates (e.g.
365 *N*-tetradecanoyl- and *N*-pentadecanoyl HSL) were enriched. Changes in fatty amides were
366 associated with both *clsA* and *clsB* deletions, with many metabolites showing opposing trends
367 between mutant strains. Levels of several *N*-acyl amides were affected by both *clsA* and *clsB*
368 deletion, including *N*-hexadecyl-L-hydroxyproline, *N*-(3-hydroxy-14-methyldecanoyl) glycine, *N*-
369 palmitoyl threonine, and *N*-stearoyl tryptophan. Some *N*-acyl amides showed gene specific
370 changes such as *N*-(3-hydroxy-1-oxodecanoyl) glycine, which was primarily affected by *clsA*
371 deletion, and *N*-palmitoyl GABA, which was impacted by *clsB* deletion (Fig. 8F). *N*-acyl amides
372 may serve as additional carbon sources and/or signaling molecules between bacteria or to the
373 host, such as through G-protein coupled receptors (GPCRs) (80, 81). Molecular network analysis
374 identified *N*-acyl amides in larger clusters of chemically similar but unannotated metabolites,
375 suggesting that *cls* modifications may lead to larger global metabolomic shifts (Fig. S9). These
376 findings demonstrate that cardiolipin synthases play essential non-redundant roles in maintaining
377 metabolic homeostasis in *B. fragilis* P207.
378

379 **DISCUSSION**

380 In this study, we demonstrate that *B. fragilis* P207 has two functionally non-redundant
381 cardiolipin synthases, which we named ClsA and ClsB. Deleting either gene leads to distinct
382 defects in *B. fragilis* fitness under stress, with the loss of *clsB* generally being more detrimental
383 than *clsA* (Fig. 9). We note that *clsA* deletion results in elevated *clsB* expression, which may
384 partially compensate for and minimize the impact of its loss. We present evidence that ClsA and
385 ClsB synthesize cardiolipin species that differ in acyl chain length and unsaturation levels,

386 suggesting that each enzyme has unique substrate specificity and contributes distinct lipids to the
387 membrane. Furthermore, loss of either enzyme has knock-off effects on diverse cellular metabolic
388 processes.

389 This study is significant for several reasons. First, we offer an approach that integrates
390 metallomics-, lipidomics-, metabolomics-, and classical genetics-based techniques to investigate
391 cardiolipin synthase function. We employ tandem mass spectrometry to assess how *cls* deletion
392 affects the lipid composition of the *B. fragilis* envelope. To our knowledge, previous studies have
393 not leveraged high-resolution mass detection to differentiate the specific lipid species produced
394 by individual Cls proteins (26, 31, 41, 42, 82). While some have used MS/MS to characterize
395 membranes of diverse taxa, including *Bacteroides*, these approaches have not been applied to
396 strains with deletion of individual *cls* genes, limiting the identification of products associated with
397 each enzyme (76, 77, 83-86). By combining genetic and analytical approaches, we distinguish
398 the unique contributions of each Cls to the cardiolipin pool and intracellular ion gradient
399 homeostasis. Second, we provide functional characterization of *cls* genes in the *Bacteroides*
400 taxonomic group, particularly genes from a novel clinical isolate from the IBD gut. As important
401 members of the human gut ecosystem, *Bacteroides* species play key roles in microbiota
402 metabolism and host immune health (46). Understanding how these microbes regulate membrane
403 composition and homeostasis is essential for understanding their fitness in the context of the gut.
404 Future research should continue to explore cardiolipin biosynthesis in these organisms,
405 particularly in *B. thetaiotaomicron*, which possesses an additional *cls* not found in most other
406 *Bacteroides* species.

407 Due to the high diversity of bacterial *cls* genes, we struggled with the best approach to
408 name the *Bacteroides* group *cls* homologs (34, 82, 87, 88). While new letter codes (e.g. *clsX* or
409 *clsN*) might help distinguish *cls* gene diversity across bacteria, this naming scheme might have
410 become onerous upon characterization of other homologs. We therefore decided on the naming

411 conventions used for *E. coli cls* and other taxa, acknowledging that *cls* homologs across different
412 bacterial phyla may have distinct functional roles (89, 90).

413 The *B. fragilis cls* genes have some similarity to *E. coli clsA* and *clsB* as the genes from
414 both taxa have strong alignment with cardiolipin synthase domain models. However, at the amino
415 acid sequence level, no clear phylogenetic relationship exists between these homologs. In each
416 taxon, the ClsA homolog is predicted to have two N-terminal transmembrane helices. While these
417 domains in ClsA are thought to be cleaved post-translationally in *E. coli*, it is likely that this does
418 not occur in *Bacillus subtilis* (26, 90). Therefore, the functional consequences of these putative
419 transmembrane domains in *B. fragilis* remain unknown, particularly their role in the cellular
420 localization of these enzymes (90, 91). In addition, across these two taxa, the *cls* expression
421 profiles are distinct. *E. coli* relies almost exclusively on *clsA* during log phase, and expression of
422 *clsB* and *clsC* is largely limited to the stationary phase (26, 31, 41, 42). Under our growth
423 conditions, *B. fragilis* expresses both *cls* genes during log phase, with *clsA* expression further
424 enhanced during stationary phase. To determine if the two *B. fragilis* Cls have overlapping
425 enzymatic activities with the Cls of these other taxa, comparative biochemical analysis of the lipid
426 products produced by the Cls homologs of each species is needed.

427 Maintaining ion gradients across membranes is essential for bacterial survival, as these
428 gradients provide a reservoir of potential energy. The loss of cardiolipin biosynthesis under non-
429 stressed conditions largely does not affect ion homeostasis, as seen in our *B. fragilis* metallomic
430 studies. Bacteria generally tightly regulate intracellular K^+ content due to its physiological
431 importance, with some adjusting it by several fold depending on extracellular conditions (24, 92).
432 For example, *B. subtilis* and *E. coli* both increase intracellular K^+ levels in response to elevated
433 osmolarity (93, 94). However, *S. aureus* does not modulate K^+ content in this manner (95). While
434 one might expect ion gradient perturbations given previous work showing improved membrane
435 stability with the presence of cardiolipin (88, 96, 97), the resilience of intracellular K^+ and Na^+
436 levels in the absence of cardiolipin suggests that otherwise unperturbed cells maintain membrane

437 integrity. Even if loss of cardiolipin changed the inherent membrane permeability of either K^+ or
438 Na^+, our data indicate that *B. fragilis* leverages membrane remodeling and several compensatory
439 ion shuttling systems to achieve and maintain intracellular homeostasis (Fig. 5C-D) (24, 92, 98-
440 103).

441 While *B. fragilis clsA* is not essential and may even diminish fitness during selective ion
442 permeabilization, both *cls* genes are beneficial when the bacterium faces broader membrane
443 stress conditions. Although unlikely, the absence of ClsA-associated cardiolipins in the Δ*clsA*
444 strain may provide stress resistance by impairing ionophore translocation across the membrane
445 (59, 104, 105). Our favored hypothesis is that Δ*clsA*-dependent membrane remodeling enhances
446 resilience to ion gradient loss, possibly through altered membrane protein or lipid function. Beyond
447 general effects like membrane fluidity, cardiolipins can influence bacterial physiology through
448 multiple pathways. For example, some proteins that influence cell shape and cell division, such
449 as the actin homolog MreB, rely on cardiolipin for proper folding at the membrane (106, 107).
450 Interactions of cardiolipin with membrane-bound or membrane-associated cell division/shape
451 proteins may also underlie our observation that the loss of cardiolipin biosynthesis results in *B.*
452 *fragilis* cell shape defects (60-66). The cls-specific cell size effects may be shaped by
453 asymmetrical distribution of cardiolipin species across inner and outer leaflets of the inner
454 membrane as well as inner leaflet of the outer membrane (16, 108-110).

455 The catalytic products of *B. fragilis* ClsA and ClsB, as inferred from our lipidomics data,
456 have distinct acyl chain lengths and unsaturation levels. In response to environmental changes,
457 bacteria can adjust these lipid properties, which are key factors influencing membrane fluidity and
458 permeability (111). For example, under conditions that increase membrane rigidity, such as lower
459 temperature or high pressure, microbes increase the abundance of highly unsaturated fatty acids
460 to restore membrane fluidity (112, 113). Exposure to membrane destabilizing agents, such as
461 alcohols, can result in decreased acyl chain unsaturation (114). Exposure to phenols, which can
462 also disrupt membranes, cause some anaerobes to increase their membrane fluidity by

463 incorporating fatty acids with trans-double bonds (115). Although *B. fragilis* apparently lacks
464 enzymes required for this particular mechanism of introducing double bonds, phylogenetically
465 diverse bacteria have other regulatory mechanisms for the introduction of double bonds into acyl
466 chains already present in the membrane (116, 117). Having two unique pools of cardiolipins with
467 corresponding membrane lipids that respond to cardiolipin fluctuations, such as hexosylceramide
468 for ClsA and *N*-acyl glycylserine for ClsB, would provide bacteria like *B. fragilis* with greater
469 adaptability in the face of diverse selective pressures in the gut.

470 The distinct metabolomic alterations observed in *B. fragilis* ClsA and ClsB mutants
471 underscore the non-redundant and critical roles of cardiolipin synthases in bacterial metabolic
472 homeostasis. Our results demonstrate that loss of either ClsA or ClsB leads to unique changes in
473 the abundance of key lipid and non-lipid metabolites. These changes likely reflect the broader
474 disruptions in membrane composition and cellular signaling, as well as shifts in central metabolic
475 pathways. Importantly, the non-additive nature of the double mutant phenotype suggests that ClsA
476 and ClsB may influence partially overlapping yet distinct biosynthetic networks. The pronounced
477 depletion and enrichment of specific metabolites, such as lipid-conjugated HSLs and *N*-acyl
478 amides, further indicates that cardiolipin synthase activity influences both membrane structure
479 and intercellular communication. Given the essential role of membrane integrity and metabolic
480 adaptability in bacterial survival within the gut environment, these findings suggest that ClsA and
481 ClsB are pivotal for the ecological fitness of *B. fragilis*.

482 In summary, *B. fragilis* relies on cardiolipin synthases to maintain barrier integrity against
483 diverse stresses that it encounters in the gut, such as bile acids and osmotic variation. However,
484 much remains to be discovered regarding *B. fragilis* Cls-mediated physiology, including protein
485 domain function, cellular localization, and the mechanism by which each enzyme produces
486 distinct cardiolipins. Furthermore, the overlapping, yet possibly distinct, functional roles that this
487 diverse enzyme class plays across the prokaryotic tree of life is ripe with potential. The data we
488 present here serve as a foundation for a deeper understanding of *B. fragilis* physiology specifically

489 as well as that of the Bacteroidota generally, potentially leading to the engineering of probiotic gut
490 species with improved gut fitness and therapeutic outcomes.
491

492 **METHODS (see supplemental methods for additional detail)**

493 ***Bacterial Growth and Strains***

494 *Strain generation*

495 *E. coli* strains were grown aerobically at 37˚ C in Miller LB broth. As appropriate, E. coli
496 cultures were supplemented with filter-sterilized 300 μM diaminopimelic acid (Sigma-Aldrich) to
497 grow auxotrophic strains and/or 100 μg/ml carbenicillin to select for plasmid containing cells. All
498 *B. fragilis* strains were grown in supplemented brain heart infusion (BHIS) medium. As
499 appropriate, cultures were supplemented with 5 μg/mL erythromycin for vector selection, 100
500 ng/mL anhydrotetracycline (aTC) for inducible ssbfe1 counter-selection (118) and 50 ng/mL aTC
501 to induce expression from aTC-inducible complementation vectors (118). *B. fragilis* strains were
502 manipulated aerobically and grown at 37˚C in an anaerobic chamber (Coy Laboratory Products)
503 filled with 5% CO_2, 2.5% hydrogen and 92.5% nitrogen.

504 Mutant strains were generated by allelic exchange using modified vectors described
505 previously (118). For conjugation into *B. fragilis* P207, plasmids were transformed into the donor
506 *E. coli* strain WM3064. Allele exchange was conducted as previously described (118). The Δ*clsA*
507 mutant (lacking ptos_000612) was complemented by integration of an aTC-inducible *clsA*
508 construct. The Δ*clsB* mutant (lacking ptos_003215) was complemented by integration of *clsB*
509 under the control of a constitutive *Bacteroides* promoter (P_{rpoD}, bt_1311/BT_RS06635).
510 Complementation constructs were integrated into the chromosome at the *att* site using an intN1
511 integrase (119). Primers, vectors, and strains are listed in Tables S1–3, respectively.
512

513 ***Cls conservation analysis***

514 *Alignment.* The *B. fragilis* P207 ClsA and ClsB gene and protein sequences, as well as *E.*
515 *coli* K-12 MG1655 (NC_000913) ClsA, ClsB, and ClsC were aligned using default settings of the
516 Geneious alignment algorithm (Geneious Prime 2024) (51, 52).

517 *DeepTMHMM*. The ClsA and ClsB amino acid sequences from *B. fragilis* P207 and *E. coli*
518 K-12 MG1655 were uploaded to DeepTMHMM (v. 1.0.42, https://dtu.biolib.com/DeepTMHMM) to
519 predict transmembrane domains (120).

520 *Inter-Phylum Tree.* Representative taxa were selected from the top five phyla in the human
521 gut (metadata listed in Table S3) (121, 122). Annotated *cls* genes were obtained from genomes
522 on NCBI and protein aligned in Geneious. One genome per species was used, aside from the two
523 *B. fragilis* strains. The phylogenetic tree was reconstructed using neighbor-end joining via
524 Geneious and then visualized using R.

525 *Intra*-Bacteroides *Tree.* TIGR04265 domains in *B. fragilis* ClsA and ClsB were identified
526 using the conserved domain database of NCBI (123). *Bacteroides* protein sequences containing
527 this domain were obtained by querying the Interpro database. Alignment, tree reconstruction, and
528 tree visualization were performed as with the inter-phylum tree, except that *E. coli* K-12 MG1655
529 ClsA was specified as an outgroup.

530 *Genomic Neighborhoods.* WebFlags2 was used to query genomic neighborhoods around
531 *B. fragilis* P207 *clsA* and *clsB* genes (124).

532

533 ***Growth curve assays***

534 Stationary phase *B. fragilis* strain cultures were back-diluted to an optical density at 600
535 nm (OD_{600}) of 0.05 and grown to OD_{600} 0.3 in the presence of 50 ng/mL aTC inducer. Each strain
536 was then diluted again to 0.025–0.05 for growth curves in a 96-well plate format. OD_{600} was
537 measured with a Tecan Infinite M Nano plate reader (Tecan, Männedorf, Switzerland) for 24 h.
538 Three biological replicates, each in technical triplicate, were performed for each growth condition.

539 To expose cells to stress conditions, BHIS medium was prepared as above but modified.
540 For pH assays, cells were pelleted and then resuspended in aTC-containing BHIS medium
541 adjusted to the appropriate pH. For deoxycholate and SDS assays, 0.01% (w/v) deoxycholate
542 (Sigma) or 0.002% (w/v) SDS (Lab Scientific) was added to cultures from filter-sterilized 1% (w/v)
543 stocks dissolved in UltraPure water. For Na^+ and K^+ assays, NaCl (Fisher Scientific) and KCl
544 (Fisher Scientific) were dissolved to a 4× concentration of each cation in BHIS medium and then
545 filter sterilized before being added to cells to yield the final concentration of cells and cation (i.e.,
546 300 mM). To determine how much additional NaCl or KCl to add, the average Na^+ and K^+ content
547 of our BHIS medium was determined using ICP-MS (see below for methods), yielding 130 mM
548 for Na^+ and 33 mM for K^+ (Table S5). For ionophore assays, a concentrated ionophore (monensin
549 A or nigericin; Sigma-Aldrich) was added to cultures to yield final concentrations of 0.8 µg/mL
550 monensin A or 0.1 µg/mL nigericin, with equivalent volumes of ethanol added to non-treated
551 conditions as a vehicle control. We calculated maximum OD600 and doubling time using R
552 (ipolygrowth; see supplemental methods) (125).
553
554 ***Microscopy***
555 *B. fragilis* P207 cell cultures were grown overnight under antibiotic selection and then
556 back-diluted into medium containing inducer (aTC) without antibiotic selection to reach log-phase
557 growth. All cultures were removed from the 37ºC incubator but were maintained under anaerobic
558 conditions, with only two or three cultures removed for microscopy at a time. Cells were visualized
559 by phase-contrast microscopy on a Leica DMI6000 B inverted microscope with a Hamamatsu
560 ORCA-R2 10600 camera with a 63× Plan Apo objective (126). Each strain was visualized on four
561 different days to generate four biological replicates. The two images per replicate from each
562 strain/day were chosen for analysis. Chosen images were processed using the MicrobeJ plugin
563 (v. 5.13I) cell size analysis software in Fiji (v. 1.54k) (127). Called cells were manually curated and

564 resulting cell lengths and widths were exported and analyzed in R to calculate cell volume and
565 Epanechnikov kernel densities.
566
567 ***Gene expression assays***
568 *Stress condition exposure*: For comparison of *cls* gene expression at log and stationary
569 phases, *B. fragilis* WT, Δ*clsA* and Δ*clsB* strain log phase cultures were back diluted to an OD_{600}
570 of 0.05 without inducer. Two and 24 h later, cell samples were pelleted and resuspended in 1 mL
571 of Trizol (Invitrogen). For acute toxicity assays, back-diluted WT *B. fragilis* cultures that reached
572 OD_{600} ~0.3–0.5 were exposed to a specified condition (i.e., pH, SDS, deoxycholate, K^+, monensin
573 A, or nigericin, as described for the growth assays) and incubated for 20 min before cell sample
574 collection.
575 *RNA extraction*: RNA was extracted as described previously (51). RNeasy Extraction Kit
576 (Qiagen) was used to treat samples with Turbo DNase (Invitrogen) using the manufacturers
577 protocol.
578 *RT-qPCR*: Samples were run in technical triplicate. *Ct* values were determined using a
579 QuantStudio5 (Applied Biosystems) instrument and a Luna One-Step RT-qPCR kit (NEB) for
580 target genes in each sample (51). Using *B. fragilis dnaN* (ptos_002600, encoding DNA
581 polymerase subunit beta) as a normalization gene.
582
583 ***Inductively coupled plasma mass spectrometry***
584 Log phase cells were removed from the anaerobic chamber for sample collection. If
585 exposed to a stress, cells were incubated for 20 min aerobically at room temperature with either
586 0.01% (w/v) deoxycholate, 0.8 µg/mL monensin A or 0.1 µg/mL nigericin. Cultures were spiked
587 with gadolinium-DOTA (Gd-DOTA, Macrocyclics) to a final concentration of 40 µM. Washing cells,
588 even with the BHIS medium cells were grown in, perturbs intracellular concentrations of small

589 alkali metals like Na^+ and K^+ making quantification difficult (Fig. S5A). Using a Gd-DOTA spike
590 enabled us to remove washing steps in the ICP-MS sample preparation process (128, 129).
591 For the wash experiment, wash condition cells were washed twice with either 250 mM
592 sucrose or BHIS media. Then, unwashed cells (i.e., no previous centrifugation) and resuspended
593 washed cells were transferred to a metal-free tube, given a Gd-DOTA spike to 40 μM, and then
594 pelleted. For *cls* and treatment comparison experiments, cells were unwashed.
595 Weighed cell pellets and supernatant were dried overnight, then digested using 70% HNO_2
596 acid, before diluting to 3% nitric acid. All standards, blanks, and ICP-MS samples were prepared
597 using ultra-trace metal grade nitric acid (70%, Fisher), ultrapure water (Millipore), metal free
598 polypropylene conical tubes (15 and 50 mL, Labcon), and trace metal grade pipette tips (Labcon).
599 All solutions were weighed for accurate elemental determination using the XSR205 DU semi-
600 analytical balance (Mettler Toledo).
601 Samples were analyzed using an Agilent 8900 Triple Quadrupole ICP-MS (Agilent
602 Technologies). To prepare ICP-MS standards, the multi element standard IV-65024 (Inorganic
603 Ventures) was diluted with 3% (v/v) nitric acid in ultrapure water. Internal standardization was
604 accomplished inline using a 200 ppb internal standard solution in 3% (v/v) nitric acid in ultrapure
605 water (IV-ICPMS-71D, Inorganic Ventures). The isotopes selected for analysis were ^{23}Na, ^{31}P, ^{32}S,
606 ^{39}K and ^{157}Gd with ^{45}Sc, ^{89}Y, ^{115}In, and ^{159}Tb used for internal standardization. For accurate
607 quantification of ^{31}P and ^{32}S, these isotopes were measured in the oxygen mode. To quantify
608 intracellular elemental concentration, the average strain-specific cell volume was determined and
609 then the molar concentration calculated for each element from the number of atoms per cell. The
610 ΔmM concentrations were calculated by subtracting the concentration of an element in the
611 medium from that in the intracellular space.
612
613 ***Lipidomics assays***

614 WT, Δ*clsA*, Δ*clsB*, and Δ*clsA* Δ*clsB* strains were backdiluted, grown to OD_{600} 0.7, and then
615 submitted on dry ice to the University of Tennessee-Knoxville Biological and Small Molecule Mass
616 Spectrometry Core (BSMMSC; RRID: SCR_021368) for targeted lipidomic analysis of membrane
617 lipids. Lipids were extracted as previously described (see supplemental methods for details) (130,
618 131). The lipidomic analyses were performed using a previously validated method (131) on an
619 ultra high performance liquid chromatography system coupled to a high resolution mass
620 spectrometer (UHPLC-HRMS). The chromatographic separations were carried out using
621 Vanquish Horizon LC system (Thermo Scientific) and reversed phase separations as described
622 previously (131). The eluent was introduced to an Exploris 120 mass spectrometer (Thermo
623 Scientific) via electrospray ionization for high resolution analysis. Following the analysis, the lipids
624 were annotated and the peak area integrated using MS-DIAL (132-135). Peak area for a
625 metabolite was first normalized to the optical density of a sample, then relative lipid abundance
626 was determined by normalizing to the total peak area of all lipids detected in each
627 UHPLC−MS/HRMS mode (i.e., positive versus negative). Elastic net regression performed using
628 the glmnet R package (136, 137).
629
630 ***Metabolomic assays***
631 WT, Δ*clsA*, Δ*clsB*, and Δ*clsA* Δ*clsB* strains were grown in 50mL BHIS medium and
632 metabolites were extracted with ethyl acetate (see supplemental methods for details). Untargeted
633 metabolomics data was acquired using a Bruker timsTOF Pro2 (Bruker-Daltonics, Billerica, MA,
634 USA) coupled to an Agilent 1290 Infinity II Bio UHPLC (Agilent, Santa Clara, CA, USA). The
635 chromatographic separations were carried out using an Acquity UPLC HSST3 column (2.1 x
636 150mm, 1.8 μM) (see supplemental methods for details). Following data acquisition, mass
637 spectrometry (MS) data were pre-processed using Bruker MetaboScape® version 9.0.1 (Bruker-
638 Daltonics, Billerica, MA, USA) and filtered using mpactR (see supplemental methods for details)
639 (138). Peak intensity for each metabolite was normalized to the total peak intensity of all features

640 detected in the sample. Molecular networking was generated as previously described (139) using
641 GNPS2: Global Natural Products Social Molecular Networking 2 (http://gnps2.org/). A minimum
642 cosine similarity score of 0.7 with at least six matching peaks, parent mass tolerance of 2 Da, and
643 fragment ion tolerance 0.5 Da were selected to generate consensus spectra. Files were imported
644 into CytoScape 3.10.3 and nodes were arranged with yFiles organic layout plugin (140). Pathway
645 analysis was performed with MetaboAnalyst 6.0 functional analysis [LC-MS] module (141). A
646 formatted peak intensity table was uploaded to the web server (https://metaboanalyst.ca), then
647 normalized by sum and log transformed. Default setting of 5.0 ppm mass tolerance, mummichog
648 algorithm v2.0 with p-value cutoff of 0.0005, against the lipid and non-lipid pathway libraries with
649 at least 3 entries in each pathway. Metabolites from enriched pathways were plotted using R
650 (v4.5.0).
651
652
653 ***Data analysis and reproducibility***
654 All data analyses were performed using R (v4.3.3 unless otherwise specified) and several
655 packages (125, 136, 137, 142-164). Code used and original datasets for all data analysis and
656 figure generation, except for the WebFlags neighborhoods, is published on GitHub
657 (https://github.com/mschnizlein/bfrag_cardiolipin). Lipidomics data alongside appropriate
658 metadata were deposited on MetaboLights (MTBLS11891
659 www.ebi.ac.uk/metabolights/MTBLS11891) (165). Untargeted metabolomics were deposited to
660 MassIVE (https://massive.ucsd.edu) (deposit in progress at time of submission).
661
662 **Acknowledgements**

663 We would like to thank the Biological and Small Molecule Mass Spectrometry Core (BSMMSC)
664 at the University of Tennessee-Knoxville and the Q-Beam Center at Michigan State University for

their work processing and analyzing samples for lipid and elemental analyses, respectively. We thank Drs. Kiwon Ok, Keith MacRenaris and Aaron Sue from the O'Halloran Lab for their advice on using the ICP-MS an analyzing output. We also would like to thank the entire Crosson Lab for their advice as the project progressed, particularly Dr. Melene Alakavuklar for her feedback on this manuscript and figure presentation, respectively. We used Biorender to generate the model presented in Figure 9. We thank two undergrads who piloted several experiments: Damone Charleston and Timothy Baldwin. We thank Kathryn McBride for strain culturing in the Balunas Lab. *E. coli* strain WM3064 was a gift from William Metcalf at UIUC. Work on this project in the S.C. lab was supported in part by NIDDK (RC2DK122394) and NIGMS (R35GM131762), in the T.V.O lab by NIGMS (P41GM135018), and in the M.J.B. lab by NCI (U01CA264071).

676 **REFERENCES**

677 1. Schnizlein MK, Young VB. 2022. Capturing the environment of the *Clostridioides difficile*
678 infection cycle. Nature Reviews Gastroenterology & Hepatology 19:508-520.
679 2. Shortt C, Hasselwander O, Meynier A, Nauta A, Fernández EN, Putz P, Rowland I,
680 Swann J, Türk J, Vermeiren J, Antoine J-M. 2018. Systematic review of the effects of the
681 intestinal microbiota on selected nutrients and non-nutrients. European Journal of
682 Nutrition 57:25-49.
683 3. Kern L, Abdeen SK, Kolodziejczyk AA, Elinav E. 2021. Commensal inter-bacterial
684 interactions shaping the microbiota. Current Opinion in Microbiology 63:158-171.
685 4. Runge S, Rosshart SP. 2021. The mammalian metaorganism: A holistic view on how
686 microbes of all kingdoms and niches shape local and systemic immunity. Frontiers in
687 Immunology 12.
688 5. He X, McLean JS, Guo L, Lux R, Shi W. 2014. The social structure of microbial
689 community involved in colonization resistance. ISME J 8:564-574.
690 6. Wennerström H, Oliveberg M. 2022. On the osmotic pressure of cells. QRB Discovery
691 3:e12.
692 7. Denyer SP, Maillard JY. 2002. Cellular impermeability and uptake of biocides and
693 antibiotics in Gram-negative bacteria. Journal of Applied Microbiology 92:35S-45S.
694 8. Zhang Y-M, Rock CO. 2008. Membrane lipid homeostasis in bacteria. Nature Reviews
695 Microbiology 6:222-233.
696 9. Strahl H, Errington J. 2017. Bacterial membranes: Structure, domains, and function.
697 Annual Review of Microbiology 71:519-538.
698 10. Sohlenkamp C, Geiger O. 2015. Bacterial membrane lipids: Diversity in structures and
699 pathways. FEMS Microbiology Reviews 40:133-159.
700 11. Blevins MS, James VK, Herrera CM, Purcell AB, Trent MS, Brodbelt JS. 2020.
701 Unsaturation elements and other modifications of phospholipids in bacteria: New insight
702 from ultraviolet photodissociation mass spectrometry. Analytical Chemistry 92:9146-
703 9155.
704 12. Roy H, Dare K, Ibba M. 2009. Adaptation of the bacterial membrane to changing
705 environments using aminoacylated phospholipids. Molecular Microbiology 71:547-550.
706 13. Cox E, Michalak A, Pagentine S, Seaton P, Pokorny A. 2014. Lysylated phospholipids
707 stabilize models of bacterial lipid bilayers and protect against antimicrobial peptides.
708 Biochimica et Biophysica Acta (BBA) - Biomembranes 1838:2198-2204.
709 14. Donohue TJ, Cain BD, Kaplan S. 1982. Alterations in the phospholipid composition of
710 *Rhodopseudomonas sphaeroides* and other bacteria induced by Tris. Journal of
711 Bacteriology 152:595-606.
712 15. Lin T-Y, Weibel DB. 2016. Organization and function of anionic phospholipids in bacteria.
713 Applied Microbiology and Biotechnology 100:4255-4267.
714 16. Bogdanov M, Pyrshev K, Yesylevskyy S, Ryabichko S, Boiko V, Ivanchenko P, Kiyamova
715 R, Guan Z, Ramseyer C, Dowhan W. 2020. Phospholipid distribution in the cytoplasmic
716 membrane of Gram-negative bacteria is highly asymmetric, dynamic, and cell shape-
717 dependent. Science Advances 6:eaaz6333.
718 17. Poolman B. 2023. Physicochemical homeostasis in bacteria. FEMS Microbiology
719 Reviews 47.
720 18. Zharova TV, Grivennikova VG, Borisov VB. 2023. $F_1 \cdot F_o$ ATP synthase/ATPase:
721 Contemporary view on unidirectional catalysis. International Journal of Molecular
722 Sciences 24:5417.
723 19. Haddock BA, Jones CW. 1977. Bacterial respiration. Bacteriol Rev 41:47-99.
724 20. Lu Z, Imlay JA. 2021. When anaerobes encounter oxygen: Mechanisms of oxygen
725 toxicity, tolerance and defence. Nature Reviews Microbiology 19:774-785.

21. Ito T, Gallegos R, Matano LM, Butler NL, Hantman N, Kaili M, Coyne MJ, Comstock LE, Malamy MH, Barquera B. 2020. Genetic and biochemical analysis of anaerobic respiration in *Bacteroides fragilis* and its importance *in vivo*. mBio 11:e03238-19.
22. Butler NL, Ito T, Foreman S, Morgan JE, Zagorevsky D, Malamy MH, Comstock LE, Barquera B. 2023. *Bacteroides fragilis* maintains concurrent capability for anaerobic and nanaerobic respiration. Journal of Bacteriology 205:e00389-22.
23. Beagle SD, Lockless SW. 2021. Unappreciated roles for K^+ channels in bacterial physiology. Trends in Microbiology 29:942-950.
24. Stautz J, Hellmich Y, Fuss MF, Silberberg JM, Devlin JR, Stockbridge RB, Hänelt I. 2021. Molecular mechanisms for bacterial potassium homeostasis. Journal of Molecular Biology 433:166968.
25. Schlame M. 2008. *Thematic Review Series: Glycerolipids.* Cardiolipin synthesis for the assembly of bacterial and mitochondrial membranes. Journal of Lipid Research 49:1607-1620.
26. Tropp BE. 1997. Cardiolipin synthase from *Escherichia coli*. Biochimica et Biophysica Acta (BBA) - Lipids and Lipid Metabolism 1348:192-200.
27. Pinkas D, Fišer R, Kozlík P, Dolejšová T, Hryzáková K, Konopásek I, Mikušová G. 2020. *Bacillus subtilis* cardiolipin protects its own membrane against surfactin-induced permeabilization. Biochimica et Biophysica Acta (BBA) - Biomembranes 1862:183405.
28. Chen Q-P, Li Q-T. 2001. Effect of cardiolipin on proton permeability of phospholipid liposomes: The role of hydration at the lipid–water interface. Archives of Biochemistry and Biophysics 389:201-206.
29. Domitin S, Puff N, Pilot-Storck F, Tiret L, Joubert F. 2025. Role of cardiolipin in proton transmembrane flux and localization. Biophysical Journal 124:408-416.
30. Shibata A, Ikawa K, Shimooka T, Terada H. 1994. Significant stabilization of the phosphatidylcholine bilayer structure by incorporation of small amounts of cardiolipin. Biochimica et Biophysica Acta (BBA) - Biomembranes 1192:71-78.
31. Jeucken A, Helms JB, Brouwers JF. 2018. Cardiolipin synthases of *Escherichia coli* have phospholipid class specific phospholipase D activity dependent on endogenous and foreign phospholipids. Biochimica et Biophysica Acta (BBA) - Molecular and Cell Biology of Lipids 1863:1345-1353.
32. Domitin S, Puff N, Pilot-Storck F, Tiret L, Joubert F. 2025. Role of cardiolipin in proton transmembrane flux and localization. Biophys J 124:408-416.
33. Shibata A, Ikawa K, Shimooka T, Terada H. 1994. Significant stabilization of the phosphatidylcholine bilayer structure by incorporation of small amounts of cardiolipin. Biochim Biophys Acta 1192:71-8.
34. Yeo W-S, Dyzenhaus S, Torres VJ, Brinsmade SR, Bae T. 2023. Regulation of bacterial two-component systems by cardiolipin. Infection and Immunity 91:e00046-23.
35. Ryabichko S, Ferreira VdM, Vitrac H, Kiyamova R, Dowhan W, Bogdanov M. 2020. Cardiolipin is required *in vivo* for the stability of bacterial translocon and optimal membrane protein translocation and insertion. Scientific Reports 10:6296.
36. Musatov A, Sedlák E. 2017. Role of cardiolipin in stability of integral membrane proteins. Biochimie 142:102-111.
37. Hong Y, Muenzner J, Grimm SK, Pletneva EV. 2012. Origin of the conformational heterogeneity of cardiolipin-bound cytochrome c. Journal of the American Chemical Society 134:18713-18723.
38. Arias-Cartin R, Grimaldi S, Arnoux P, Guigliarelli B, Magalon A. 2012. Cardiolipin binding in bacterial respiratory complexes: Structural and functional implications. Biochimica et Biophysica Acta (BBA) - Bioenergetics 1817:1937-1949.

39. Planas-Iglesias J, Dwarakanath H, Mohammadyani D, Yanamala N, Kagan Valerian E, Klein-Seetharaman J. 2015. Cardiolipin interactions with proteins. Biophysical Journal 109:1282-1294.
40. Hirschberg CB, Kennedy EP. 1972. Mechanism of the enzymatic synthesis of cardiolipin in *Escherichia coli*. Proceedings of the National Academy of Sciences 69:648-651.
41. Tan BK, Bogdanov M, Zhao J, Dowhan W, Raetz CR, Guan Z. 2012. Discovery of a cardiolipin synthase utilizing phosphatidylethanolamine and phosphatidylglycerol as substrates. Proceedings of the National Academy of Sciences 109:16504-16509.
42. Guo D, Tropp BE. 2000. A second *Escherichia coli* protein with CL synthase activity. Biochimica et Biophysica Acta (BBA) - Molecular and Cell Biology of Lipids 1483:263-274.
43. Li C, Tan BK, Zhao J, Guan Z. 2016. *In Vivo* and *in Vitro* synthesis of phosphatidylglycerol by an *Escherichia coli* cardiolipin synthase. Journal of Biological Chemistry 291:25144-25153.
44. Homma H, Nojima S. 1982. Synthesis of various phospholipids from 2-acyl lysophospholipids by *Escherichia coli* extract. The Journal of Biochemistry 91:1103-1110.
45. Patrick S. 2022. A tale of two habitats: *Bacteroides fragilis*, a lethal pathogen and resident in the human gastrointestinal microbiome. Microbiology 168.
46. Wexler HM. 2007. *Bacteroides*: The good, the bad, and the nitty-gritty. Clin Microbiol Rev 20:593-621.
47. Tally FP, Stewart PR, Sutter VL, Rosenblatt JE. 1975. Oxygen tolerance of fresh clinical anaerobic bacteria. J Clin Microbiol 1:161-4.
48. Valguarnera E, Wardenburg JB. 2020. Good Gone Bad: One Toxin Away From Disease for Bacteroides fragilis. J Mol Biol 432:765-785.
49. Scott N, Whittle E, Jeraldo P, Chia N. 2022. A systemic review of the role of enterotoxic *Bacteroides fragilis* in colorectal cancer. Neoplasia 29:100797.
50. Sun F, Zhang Q, Zhao J, Zhang H, Zhai Q, Chen W. 2019. A potential species of next-generation probiotics? The dark and light sides of *Bacteroides fragilis* in health. Food Res Int 126:108590.
51. Fiebig A, Schnizlein MK, Pena-Rivera S, Trigodet F, Dubey AA, Hennessy MK, Basu A, Pott S, Dalal S, Rubin D, Sogin ML, Eren AM, Chang EB, Crosson S. 2024. Bile acid fitness determinants of a *Bacteroides fragilis* isolate from a human pouchitis patient. mBio 15:e02830-23.
52. Vineis JH, Ringus DL, Morrison HG, Delmont TO, Dalal S, Raffals LH, Antonopoulos DA, Rubin DT, Eren AM, Chang EB, Sogin ML. 2016. Patient-specific *Bacteroides* genome variants in pouchitis. mBio 7:e01713-16.
53. Akiyama S, Rai V, Rubin DT. 2021. Pouchitis in inflammatory bowel disease: a review of diagnosis, prognosis, and treatment. Intest Res 19:1-11.
54. Sitaraman R. 2013. Phospholipid catabolism by gut microbiota and the risk of cardiovascular disease. J Med Microbiol 62:948-950.
55. Romantsov T, Gonzalez K, Sahtout N, Culham DE, Coumoundouros C, Garner J, Kerr CH, Chang L, Turner RJ, Wood JM. 2018. Cardiolipin synthase A colocalizes with cardiolipin and osmosensing transporter ProP at the poles of *Escherichia coli* cells. Molecular Microbiology 107:623-638.
56. Quigley BR, Tropp BE. 2009. *E. coli* cardiolipin synthase: Function of N-terminal conserved residues. Biochimica et Biophysica Acta (BBA) - Biomembranes 1788:2107-2113.
57. Antonenko YN, Yaguzhinsky LS. 1988. The ion selectivity of nonelectrogenic ionophores measured on a bilayer lipid membrane: Nigericin, monensin, A23187 and lasalocid A. Biochim Biophys Acta 938:125-30.

58. Li J, Ding L, Wang E, Dong S. 1996. The ion selectivity of monensin incorporated phospholipid/alkanethiol bilayers. Journal of Electroanalytical Chemistry 414:17-21.
59. Łowicki D, Huczyński A. 2013. Structure and antimicrobial properties of monensin A and its derivatives: Summary of the achievements. BioMed Research International 2013:742149.
60. Lin T-Y, Gross William S, Auer George K, Weibel Douglas B. 2019. Cardiolipin alters *Rhodobacter sphaeroides* cell shape by affecting peptidoglycan precursor biosynthesis. mBio 10.
61. Elías-Wolff F, Lindén M, Lyubartsev AP, Brandt EG. 2019. Curvature sensing by cardiolipin in simulated buckled membranes. Soft Matter 15:792-802.
62. Luchini A, Cavasso D, Radulescu A, D'Errico G, Paduano L, Vitiello G. 2021. Structural organization of cardiolipin-containing vesicles as models of the bacterial cytoplasmic membrane. Langmuir 37:8508-8516.
63. Labajová N, Baranova N, Jurásek M, Vácha R, Loose M, Barák I. 2021. Cardiolipin-containing lipid membranes attract the bacterial cell division protein DivIVA. International Journal of Molecular Sciences 22:8350.
64. Renner LD, Weibel DB. 2011. Cardiolipin microdomains localize to negatively curved regions of *Escherichia coli* membranes. Proceedings of the National Academy of Sciences 108:6264-6269.
65. Huang KC, Mukhopadhyay R, Wingreen NS. 2006. A curvature-mediated mechanism for localization of lipids to bacterial poles. PLOS Computational Biology 2:e151.
66. Bailey BWA, Stansfeld PJ. 2024. The bacterial cytoskeleton alters the cell membrane in molecular dynamics simulations. Biophysical Journal 123:374a.
67. Rowlett VW, Mallampalli VKPS, Karlstaedt A, Dowhan W, Taegtmeyer H, Margolin W, Vitrac H. 2017. Impact of membrane phospholipid alterations in *Escherichia coli* on cellular function and bacterial stress adaptation. Journal of Bacteriology 199:10.1128/jb.00849-16.
68. Duncan AL, Robinson AJ, Walker JE. 2016. Cardiolipin binds selectively but transiently to conserved lysine residues in the rotor of metazoan ATP synthases. Proc Natl Acad Sci U S A 113:8687-92.
69. Mehdipour AR, Hummer G. 2016. Cardiolipin puts the seal on ATP synthase. Proc Natl Acad Sci U S A 113:8568-70.
70. Shapiro JS, Chang H-C, Tatekoshi Y, Zhao Z, Waxali ZS, Hong BJ, Chen H, Geier JA, Bartom ET, De Jesus A, Nejad FK, Mahmoodzadeh A, Sato T, Ramos-Alonso L, Romero AM, Martinez-Pastor MT, Jiang S-C, Sah-Teli SK, Li L, Bentrem D, Lopaschuk G, Ben-Sahra I, O'Halloran TV, Shilatifard A, Puig S, Bergelson J, Koivunen P, Ardehali H. 2023. Iron drives anabolic metabolism through active histone demethylation and mTORC1. Nature Cell Biology 25:1478-1494.
71. Lane A, Gokhale A, Werner E, Roberts A, Freeman A, Roberts B, Faundez V. 2022. Sulfur- and phosphorus-standardized metal quantification of biological specimens using inductively coupled plasma mass spectrometry. STAR Protoc 3:101334.
72. Schaechter M, MaalØe O, Kjeldgaard NO. 1958. Dependency on medium and temperature of cell size and chemical composition during balanced growth of *Salmonella typhimurium*. Microbiology 19:592-606.
73. Kjeldgaard NO, MaalØe O, Schaechter M. 1958. The transition between different physiological states during balanced growth of *Salmonella typhimurium*. Microbiology 19:607-616.
74. Mulyukin AL, Sorokin VV, Loiko NG, Suzina NE, Duda VI, Vorob'eva EA, El'-Registan GI. 2002. Comparative study of the elemental composition of vegetative and resting microbial cells. Microbiology 71:31-40.

875 75. Sivakumar P, Fernández-Bravo A, Taleh L, Biddle JF, Melikechi N. 2015. Detection and
876 classification of live and dead *Escherichia coli* by laser-induced breakdown
877 spectroscopy. Astrobiology 15:144-153.
878 76. Sartorio Mariana G, Valguarnera E, Hsu F-F, Feldman Mario F. 2022. Lipidomics
879 analysis of outer membrane vesicles and elucidation of the inositol phosphoceramide
880 biosynthetic pathway in *Bacteroides thetaiotaomicron*. Microbiology Spectrum
881 10:e00634-21.
882 77. Ryan E, Gonzalez Pastor B, Gethings LA, Clarke DJ, Joyce SA. 2023. Lipidomic
883 analysis reveals differences in *Bacteroides* species driven largely by plasmalogens,
884 glycerophosphoinositols and certain sphingolipids. Metabolites 13:360.
885 78. Rizza V, Tucker Anne N, White David C. 1970. Lipids of *Bacteroides melaninogenicus*.
886 Journal of Bacteriology 101:84-91.
887 79. Withers H, Swift S, Williams P. 2001. Quorum sensing as an integral component of gene
888 regulatory networks in Gram-negative bacteria. Current Opinion in Microbiology 4:186-
889 193.
890 80. Otaru N, Ye K, Mujezinovic D, Berchtold L, Constancias F, Cornejo FA, Krzystek A, de
891 Wouters T, Braegger C, Lacroix C, Pugin B. 2021. GABA production by human intestinal
892 Bacteroides spp.: Prevalence, regulation, and role in acid stress tolerance. Frontiers in
893 Microbiology 12.
894 81. Cohen LJ, Kang HS, Chu J, Huang YH, Gordon EA, Reddy BV, Ternei MA, Craig JW,
895 Brady SF. 2015. Functional metagenomic discovery of bacterial effectors in the human
896 microbiome and isolation of commendamide, a GPCR G2A/132 agonist. Proc Natl Acad
897 Sci U S A 112:E4825-34.
898 82. Koprivnjak T, Zhang D, Ernst CM, Peschel A, Nauseef WM, Weiss JP. 2011.
899 Characterization of *Staphylococcus aureus* cardiolipin synthases 1 and 2 and their
900 contribution to accumulation of cardiolipin in stationary phase and within phagocytes.
901 Journal of Bacteriology 193:4134-4142.
902 83. Mirretta Barone C, Heaver SL, Gruber L, Zundel F, Vu DL, Ley RE. 2024. Spatially
903 resolved lipidomics shows conditional transfer of lipids produced by Bacteroides
904 thetaiotaomicron into the mouse gut. Cell Host & Microbe 32:1025-1036.e5.
905 84. An D, Na C, Bielawski J, Hannun YA, Kasper DL. 2011. Membrane sphingolipids as
906 essential molecular signals for Bacteroides survival in the intestine. Proceedings of the
907 National Academy of Sciences 108:4666-4671.
908 85. Frankfater CF, Sartorio MG, Valguarnera E, Feldman MF, Hsu F-F. 2023. Lipidome of the
909 Bacteroides Genus Containing New Peptidolipid and Sphingolipid Families Revealed by
910 Multiple-Stage Mass Spectrometry. Biochemistry 62:1160-1180.
911 86. Hines KM, Xu L. 2019. Lipidomic consequences of phospholipid synthesis defects in
912 *Escherichia coli* revealed by HILIC-ion mobility-mass spectrometry. Chemistry and
913 Physics of Lipids 219:15-22.
914 87. Czolkoss S, Fritz C, Hölzl G, Aktas M. 2016. Two distinct cardiolipin synthases operate
915 in *Agrobacterium tumefaciens*. PLOS ONE 11:e0160373.
916 88. Tsai M, Ohniwa RL, Kato Y, Takeshita SL, Ohta T, Saito S, Hayashi H, Morikawa K. 2011.
917 *Staphylococcus aureus* requires cardiolipin for survival under conditions of high salinity.
918 BMC Microbiology 11:13.
919 89. Liu J, Ryabichko S, Bogdanov M, Fackelmayer OJ, Dowhan W, Krulwich TA. 2014.
920 Cardiolipin is dispensable for oxidative phosphorylation and non-fermentative growth of
921 alkaliphilic Bacillus pseudofirmus OF4. J Biol Chem 289:2960-71.
922 90. Kusaka J, Shuto S, Imai Y, Ishikawa K, Saito T, Natori K, Matsuoka S, Hara H,
923 Matsumoto K. 2016. Septal localization by membrane targeting sequences and a
924 conserved sequence essential for activity at the COOH-terminus of *Bacillus subtilis*
925 cardiolipin synthase. Research in Microbiology 167:202-214.

91. Shibuya I, Yamagoe S, Miyazaki C, Matsuzaki H, Ohta A. 1985. Biosynthesis of novel acidic phospholipid analogs in *Escherichia coli*. Journal of Bacteriology 161:473-477.
92. Walderhaug MO, Dosch DC, Epstein W. 1987. Potassium Transport in Bacteria, p 85-130. *In* Rosen BP, Silver S (ed), Ion Transport in Prokaryotes doi:10.1016/B978-0-12-596935-2.50005-0. Academic Press.
93. Whatmore AM, Chudek JA, Reed RH. 1990. The effects of osmotic upshock on the intracellular solute pools of *Bacillus subtilis*. Microbiology 136:2527-2535.
94. Epstein W. 1986. Osmoregulation by potassium transport in *Escherichia coli*. FEMS Microbiology Reviews 2:73-78.
95. Christian JHB, Waltho JA. 1964. The composition of *Staphylococcus aureus* in relation to the water activity of the growth medium. Microbiology 35:205-213.
96. Jagannathan S. 1994. Characterization of proton and water permeability across model membrane vesicles and proteoliposomes. 9600672. Clemson University, South Carolina, USA.
97. Kato S, Tobe H, Matsubara H, Sawada M, Sasaki Y, Fukiya S, Morita N, Yokota A. 2019. The membrane phospholipid cardiolipin plays a pivotal role in bile acid adaptation by Lactobacillus gasseri JCM1131T. Biochimica et Biophysica Acta (BBA) - Molecular and Cell Biology of Lipids 1864:403-412.
98. Dimroth P. 1994. Bacterial sodium ion-coupled energetics. Antonie Van Leeuwenhoek 65:381-95.
99. Mulkidjanian AY, Dibrov P, Galperin MY. 2008. The past and present of sodium energetics: may the sodium-motive force be with you. Biochim Biophys Acta 1777:985-92.
100. Ren Q, Paulsen IT. 2009. Transport, Solute, p 529-544. *In* Schaechter M (ed), Encyclopedia of Microbiology (Third Edition) doi:10.1016/B978-012373944-5.00107-3. Academic Press, Oxford.
101. van de Vossenberg JL, Ubbink-Kok T, Elferink MG, Driessen AJ, Konings WN. 1995. Ion permeability of the cytoplasmic membrane limits the maximum growth temperature of bacteria and archaea. Mol Microbiol 18:925-32.
102. Deamer DW, Bramhall J. 1986. Permeability of lipid bilayers to water and ionic solutes. Chemistry and Physics of Lipids 40:167-188.
103. Hopfer U, Lehninger AL, Lennarz WJ. 1970. The effect of the polar moiety of lipids on the ion permeability of bilayer membranes. The Journal of Membrane Biology 2:41-58.
104. Russell JB. 1987. A proposed mechanism of monensin action in inhibiting ruminant bacterial growth: Effects on ion flux and proton motive force. Journal of Animal Science 64:1519-1525.
105. Guffanti AA, Davidson LF, Mann TM, Krulwich TA. 1979. Nigericin-induced death of an acidophilic bacterium. Microbiology 114:201-206.
106. Ouellette SP, Fisher-Marvin LA, Harpring M, Lee J, Rucks EA, Cox JV. 2022. Localized cardiolipin synthesis is required for the assembly of MreB during the polarized cell division of *Chlamydia trachomatis*. PLOS Pathogens 18:e1010836.
107. Kurita K, Kato F, Shiomi D. 2020. Alteration of membrane fluidity or phospholipid composition perturbs rotation of MreB complexes in *Escherichia coli*. Frontiers in Molecular Biosciences 7.
108. Dong H, Zhang Z, Tang X, Huang S, Li H, Peng B, Dong C. 2016. Structural insights into cardiolipin transfer from the Inner membrane to the outer membrane by PbgA in Gram-negative bacteria. Scientific Reports 6:30815-30815.
109. Bogdanov M. 2023. The power and challenge of lipid (a)symmetry across the membrane and cell. Emerging Topics in Life Sciences 7:1-6.

110. Bogdanov M. 2023. Renovating a double fence with or without notifying the next door and across the street neighbors: why the biogenic cytoplasmic membrane of Gram-negative bacteria display asymmetry? . Emerging Topics in Life Sciences 7:137-150.
111. Lande MB, Donovan JM, Zeidel ML. 1995. The relationship between membrane fluidity and permeabilities to water, solutes, ammonia, and protons. Journal of General Physiology 106:67-84.
112. Neidleman SL. 1987. Effects of temperature on lipid unsaturation. Biotechnology and Genetic Engineering Reviews 5:245-268.
113. Yano Y, Nakayama A, Ishihara K, Saito H. 1998. Adaptive changes in membrane lipids of barophilic bacteria in response to changes in growth pressure. Applied and Environmental Microbiology 64:479-485.
114. Huffer S, Clark ME, Ning JC, Blanch HW, Clark DS. 2011. Role of alcohols in growth, lipid composition, and membrane fluidity of yeasts, bacteria, and archaea. Applied and Environmental Microbiology 77:6400-6408.
115. Keweloh H, Heipieper HJ. 1996. Trans unsaturated fatty acids in bacteria. Lipids 31:129-137.
116. Altabe SG, Aguilar P, Caballero GM, de Mendoza D. 2003. The *Bacillus subtilis* acyl lipid desaturase is a delta5 desaturase. J Bacteriol 185:3228-31.
117. Schweizer HP, Choi K-H. 2011. *Pseudomonas aeruginosa* aerobic fatty acid desaturase DesB is important for virulence factor production. Archives of Microbiology 193:227-234.
118. García-Bayona L, Comstock LE. 2019. Streamlined genetic manipulation of diverse *Bacteroides* and *Parabacteroides* isolates from the human gut microbiota. mBio 10.
119. Rajeev L, Segall A, Gardner J. 2007. The *Bacteroides* NBU1 integrase performs a homology-independent strand exchange to form a holliday junction intermediate. J Biol Chem 282:31228-37.
120. Hallgren J, Tsirigos KD, Pedersen MD, Almagro Armenteros JJ, Marcatili P, Nielsen H, Krogh A, Winther O. 2022. DeepTMHMM predicts alpha and beta transmembrane proteins using deep neural networks. bioRxiv doi:10.1101/2022.04.08.487609:2022.04.08.487609.
121. Bäckhed F, Ley RE, Sonnenburg JL, Peterson DA, Gordon JI. 2005. Host-bacterial mutualism in the human intestine. Science 307:1915-1920.
122. Adak A, Khan MR. 2019. An insight into gut microbiota and its functionalities. Cellular and Molecular Life Sciences 76:473-493.
123. Lu S, Wang J, Chitsaz F, Derbyshire MK, Geer RC, Gonzales NR, Gwadz M, Hurwitz DI, Marchler GH, Song JS, Thanki N, Yamashita RA, Yang M, Zhang D, Zheng C, Lanczycki CJ, Marchler-Bauer A. 2020. CDD/SPARCLE: The conserved domain database in 2020. Nucleic Acids Res 48:D265-d268.
124. Saha CK, Sanches Pires R, Brolin H, Delannoy M, Atkinson GC. 2020. FlaGs and webFlaGs: Discovering novel biology through the analysis of gene neighbourhood conservation. Bioinformatics 37:1312-1314.
125. Wang J, Barger K. 2024. ipolygrowth: An R package to calculate individual growth curve parameters from bacterial time series data. Microbiology Resource Announcements 13:e00662-24.
126. McLaughlin M, Fiebig A, Crosson S. 2023. XRE transcription factors conserved in Caulobacter and φCbK modulate adhesin development and phage production. PLOS Genetics 19:e1011048.
127. Ducret A, Quardokus EM, Brun YV. 2016. MicrobeJ, a tool for high throughput bacterial cell detection and quantitative analysis. Nature Microbiology 1:16077.
128. Sakol N, Egawa A, Fujiwara T. 2020. Gadolinium complexes as contrast agent for cellular NMR spectroscopy. Int J Mol Sci 21:4042.

129. Aime S, Cabella C, Colombatto S, Geninatti Crich S, Gianolio E, Maggioni F. 2002. Insights into the use of paramagnetic Gd(III) complexes in MR-molecular imaging investigations. Journal of Magnetic Resonance Imaging 16:394-406.
130. Basso JTR, Jones KA, Jacobs KR, Christopher CJ, Fielland HB, Campagna SR, Buchan A. 2022. Growth Substrate and Prophage Induction Collectively Influence Metabolite and Lipid Profiles in a Marine Bacterium. mSystems 7:e0058522.
131. Woodall B, Fozo EM, Campagna SR. 2023. Dual stable isotopes enhance lipidomic studies in bacterial model organism Enterococcus faecalis. Anal Bioanal Chem 415:3593-3605.
132. Tsugawa H, Ikeda K, Takahashi M, Satoh A, Mori Y, Uchino H, Okahashi N, Yamada Y, Tada I, Bonini P, Higashi Y, Okazaki Y, Zhou Z, Zhu Z-J, Koelmel J, Cajka T, Fiehn O, Saito K, Arita M, Arita M. 2020. A lipidome atlas in MS-DIAL 4. Nature Biotechnology 38:1159-1163.
133. Tsugawa H, Nakabayashi R, Mori T, Yamada Y, Takahashi M, Rai A, Sugiyama R, Yamamoto H, Nakaya T, Yamazaki M, Kooke R, Bac-Molenaar JA, Oztolan-Erol N, Keurentjes JJB, Arita M, Saito K. 2019. A cheminformatics approach to characterize metabolomes in stable-isotope-labeled organisms. Nature Methods 16:295-298.
134. Lai Z, Tsugawa H, Wohlgemuth G, Mehta S, Mueller M, Zheng Y, Ogiwara A, Meissen J, Showalter M, Takeuchi K, Kind T, Beal P, Arita M, Fiehn O. 2018. Identifying metabolites by integrating metabolome databases with mass spectrometry cheminformatics. Nature Methods 15:53-56.
135. Tsugawa H, Cajka T, Kind T, Ma Y, Higgins B, Ikeda K, Kanazawa M, VanderGheynst J, Fiehn O, Arita M. 2015. MS-DIAL: data-independent MS/MS deconvolution for comprehensive metabolome analysis. Nat Methods 12:523-6.
136. Friedman JH, Hastie T, Tibshirani R. 2010. Regularization paths for generalized linear models via coordinate descent. Journal of Statistical Software 33:1 - 22.
137. Tay JK, Narasimhan B, Hastie T. 2023. Elastic net regularization paths for all generalized linear models. Journal of Statistical Software 106:1 - 31.
138. Mason Allison R, Johnson JG, Krampen J, Nguyen Jennifer NT, Balunas Marcy J, Schloss Patrick D. 2025. mpactR: An R adaptation of the metabolomics peak analysis computational tool (MPACT) for use in reproducible data analysis pipelines. Microbiology Resource Announcements 14:e00997-24.
139. Wang M, Carver JJ, Phelan VV, Sanchez LM, Garg N, Peng Y, Nguyen DD, Watrous J, Kapono CA, Luzzatto-Knaan T, Porto C, Bouslimani A, Melnik AV, Meehan MJ, Liu W-T, Crüsemann M, Boudreau PD, Esquenazi E, Sandoval-Calderón M, Kersten RD, Pace LA, Quinn RA, Duncan KR, Hsu C-C, Floros DJ, Gavilan RG, Kleigrewe K, Northen T, Dutton RJ, Parrot D, Carlson EE, Aigle B, Michelsen CF, Jelsbak L, Sohlenkamp C, Pevzner P, Edlund A, McLean J, Piel J, Murphy BT, Gerwick L, Liaw C-C, Yang Y-L, Humpf H-U, Maansson M, Keyzers RA, Sims AC, Johnson AR, Sidebottom AM, Sedio BE, et al. 2016. Sharing and community curation of mass spectrometry data with Global Natural Products Social Molecular Networking. Nature Biotechnology 34:828-837.
140. Shannon P, Markiel A, Ozier O, Baliga NS, Wang JT, Ramage D, Amin N, Schwikowski B, Ideker T. 2003. Cytoscape: A software environment for integrated models of biomolecular interaction networks. Genome Res 13:2498-504.
141. Pang Z, Lu Y, Zhou G, Hui F, Xu L, Viau C, Spigelman Aliya F, MacDonald Patrick E, Wishart David S, Li S, Xia J. 2024. MetaboAnalyst 6.0: Towards a unified platform for metabolomics data processing, analysis and interpretation. Nucleic Acids Research 52:W398-W406.
142. Team RDC. 2013. R: A language and environment for statistical computing, R Foundation for Statistical Computing, http://www.R-project.org/.

143. Wickham H. 2016. ggplot2: Elegant graphics for data analysis, Springer-Verlag, New York. https://ggplot2.tidyverse.org.
144. Wong B. 2011. Points of view: Color blindness. Nature Methods 8:441-441.
145. Ou J. 2021. colorBlindness: Safe color set for color blindness, https://CRAN.R-project.org/package=colorBlindnes.
146. Neuwirth E. 2022. RColorBrewer: ColorBrewer palettes, https://CRAN.R-project.org/package=RColorBrewer.
147. Vu VQ, Friendly M. 2024. ggbiplot: A grammar of graphics implementation of biplots, https://CRAN.R-project.org/package=ggbiplot.
148. Pedersen TL. 2024. ggforce: Accelerating 'ggplot2', https://CRAN.R-project.org/package=ggforce.
149. Gu Z, Gu L, Eils R, Schlesner M, Brors B. 2014. circlize implements and enhances circular visualization in R. Bioinformatics 30:2811-2.
150. Gu Z, Eils R, Schlesner M. 2016. Complex heatmaps reveal patterns and correlations in multidimensional genomic data. Bioinformatics 32:2847-9.
151. Neitmann T. 2020. mdthemes: Markdown themes for 'ggplot2', https://CRAN.R-project.org/package=mdthemes.
152. C W, B W. 2022. ggtext: Improved text rendering support for 'ggplot2', https://CRAN.R-project.org/package=ggtext.
153. Wickham H, Bryan J. 2023. readxl: Read excel files, https://CRAN.R-project.org/package=readxl.
154. Wickham H, Vaughan D, Girlich M. 2024. tidyr: Tidy messy data, https://CRAN.R-project.org/package=tidyr.
155. Bengtsson H. 2024. matrixStats: Functions that apply to rows and columns of matrices (and to vectors), https://CRAN.R-project.org/package=matrixStats.
156. Barrett T, Dowle M, Srinivasan A, Gorecki J, Chirico M, Hocking T. 2024. data.table: Extension of `data.frame`, https://CRAN.R-project.org/package=data.table.
157. Bache SM, Wickham H. 2022. magrittr: A forward-pipe operator for R, https://cran.r-project.org/web/packages/magrittr/vignettes/magrittr.html.
158. Wickham H, Pedersen TL, Seidel D. 2023. scales: Scale functions for visualization, https://CRAN.R-project.org/package=scales.
159. Wang L-G, Lam TT-Y, Xu S, Dai Z, Zhou L, Feng T, Guo P, Dunn CW, Jones BR, Bradley T, Zhu H, Guan Y, Jiang Y, Yu G. 2019. Treeio: An R package for phylogenetic tree input and output with richly annotated and associated data. Molecular Biology and Evolution 37:599-603.
160. Yu G, Smith DK, Zhu H, Guan Y, Lam TT-Y. 2017. ggtree: An R package for visualization and annotation of phylogenetic trees with their covariates and other associated data. Methods in Ecology and Evolution 8:28-36.
161. Xu S, Li L, Luo X, Chen M, Tang W, Zhan L, Dai Z, Lam TT, Guan Y, Yu G. 2022. Ggtree: A serialized data object for visualization of a phylogenetic tree and annotation data. iMeta 1:e56.
162. Bates D, Mächler M, Bolker B, Walker S. 2015. Fitting linear mixed-effects models using lme4. J of Statistical Software 67:1-48.
163. Kuznetsova A, Brockhoff PB, Christensen RHB. 2017. lmerTest package: Tests in linear mixed effects models. J of Statistical Software 82:1-26.
164. A K. 2023. ggpubr: 'ggplot2' based publication ready plots, https://CRAN.R-project.org/package=ggpubr.

1123 165. Yurekten O, Payne T, Tejera N, Amaladoss FX, Martin C, Williams M, O'Donovan C.
1124 2023. MetaboLights: open data repository for metabolomics. Nucleic Acids Research
1125 52:D640-D646.
1126 166. Vingadassalom D, Kolb A, Mayer C, Rybkine T, Collatz E, Podglajen I. 2005. An unusual
1127 primary sigma factor in the Bacteroidetes phylum. Mol Microbiol 56:888-902.
1128 167. Loferer-Krössbacher M, Klima J, Psenner R. 1998. Determination of bacterial cell dry
1129 mass by transmission electron microscopy and densitometric image analysis. Appl
1130 Environ Microbiol 64:688-94.
1131 168. Epanechnikov VA. 1969. Non-parametric estimation of a multivariate probability density.
1132 Theory of Probability & Its Applications 14:153-158.
1133 169. Poynton EF, van Santen JA, Pin M, Contreras MM, McMann E, Parra J, Showalter B,
1134 Zaroubi L, Duncan Katherine R, Linington RG. 2024. The Natural Products Atlas 3.0:
1135 Extending the database of microbially derived natural products. Nucleic Acids Research
1136 53:D691-D699.
1137 170. Wang F, Allen D, Tian S, Oler E, Gautam V, Greiner R, Metz Thomas O, Wishart
1138 David S. 2022. CFM-ID 4.0 – a web server for accurate MS-based metabolite
1139 identification. Nucleic Acids Research 50:W165-W174.
1140 171. Conroy MJ, Andrews RM, Andrews S, Cockayne L, Dennis Edward A, Fahy E, Gaud C,
1141 Griffiths William J, Jukes G, Kolchin M, Mendivelso K, Lopez-Clavijo Andrea F, Ready C,
1142 Subramaniam S, O'Donnell Valerie B. 2023. LIPID MAPS: update to databases and
1143 tools for the lipidomics community. Nucleic Acids Research 52:D1677-D1682.

1144

1145

FIGURES AND TABLES

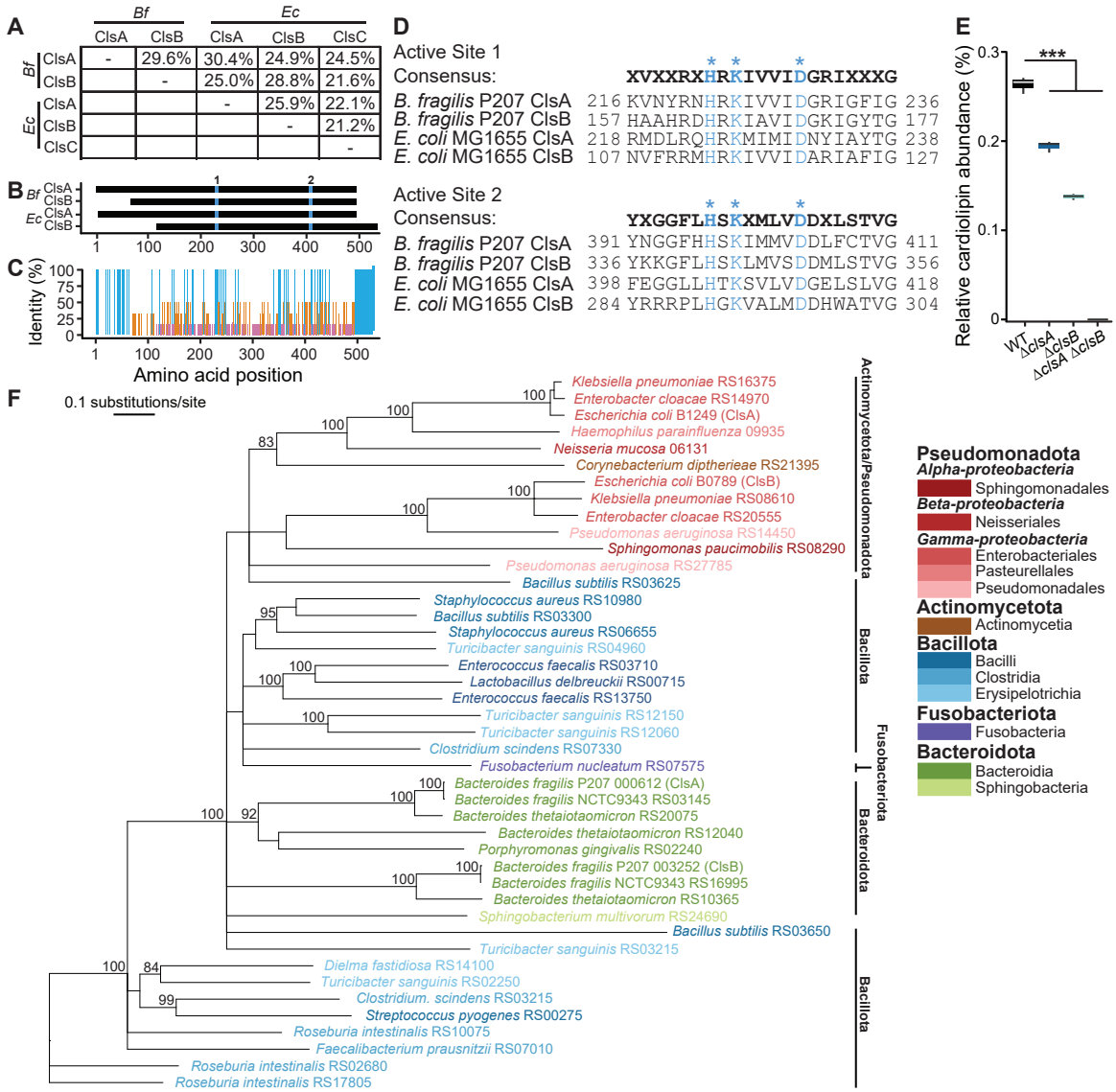

Figure 1. Cardiolipin synthases diverge across the dominant gut bacterial phyla. A. Percentage identity from pairwise amino acid alignment of cardiolipin synthases in *B. fragilis* P207 (*Bf*) and *E. coli* K12 MG1655 (*Ec*). **B.** Alignment of ClsA and ClsB from *B. fragilis* P207 and *E. coli* MG1655, with the two HKD domains marked in blue. **C.** Percentage identity from amino acid alignment in panel B colored based on the thresholds <30% (pink), <100% (orange) and 100% (blue). **D.** Consensus and individual sequences of the regions flanking the two HKD active sites of *B. fragilis* and *E. coli* Cls proteins. HKD residues are colored in blue; the N- and C-terminal positions are shown. **E.** Relative abundance of cardiolipin in *B. fragilis* P207

1155 wild-type (WT), Δ*clsA*, Δ*clsB* and Δ*clsA* Δ*clsB* strains measured by mass spectrometry. The horizontal line
1156 indicates the median, and the whiskers 1.5× the interquartile range outside the 25th and 75th percentiles of
1157 n = 3 samples. (linear regression; unadjusted p-values are shown; *** indicates $p < 0.001$). **F.** Neighbor-
1158 joining tree of a Cls alignment from representative taxa of major bacterial phyla in the gut, using only one
1159 genome per species. For each sequence in the tree, taxa names are followed by genome IDs at the tip of
1160 each branch; genome accession numbers and other metadata are provided in Table S3. Bootstrap values
1161 are shown only if >80%. Bacterial taxa are colored according to the phylum to which they belong (red,
1162 Pseudomonadota – 3 classes with 1, 1, and 3 families; brown, Actinomycetota – 1 class; blue, Bacillota –
1163 3 classes; violet, Fusobacteriota – 1 class; green, Bacteroidota – 2 classes, respectively). Key indicates the
1164 rate of amino acid substitutions per site.
1165
1166

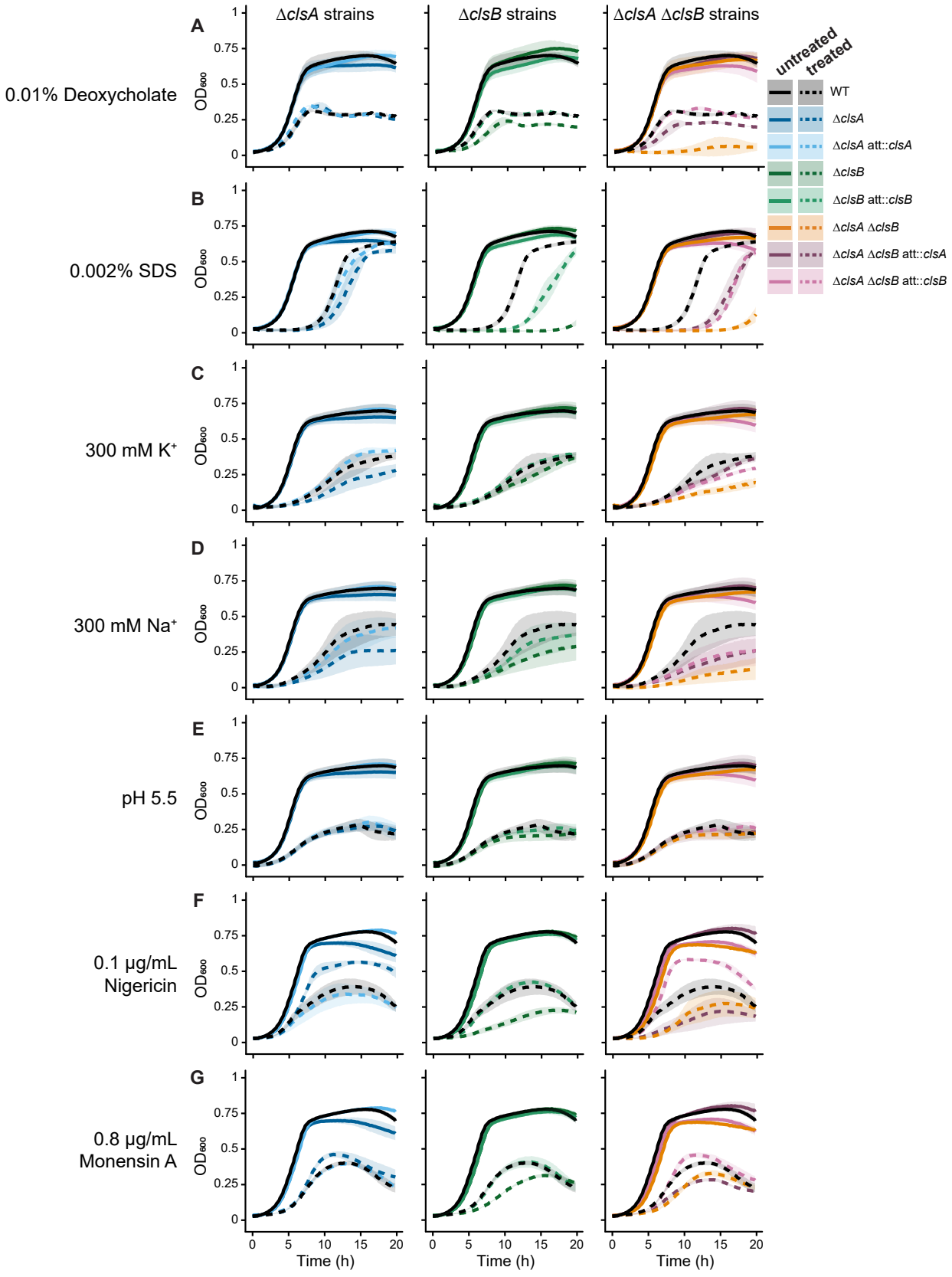
ΔclsA strains
ΔclsB strains
ΔclsA ΔclsB strains
A
B
C
D
E
F
G
0.01% Deoxycholate
0.002% SDS
300 mM K+
300 mM Na+
pH 5.5
0.1 µg/mL Nigericin
0.8 µg/mL Monensin A
OD600
Time (h)
untreated
treated
WT
ΔclsA
ΔclsA att::clsA
ΔclsB
ΔclsB att::clsB
ΔclsA ΔclsB
ΔclsA ΔclsB att::clsA
ΔclsA ΔclsB att::clsB

1167

1168 **Figure 2. Loss of cardiolipin synthase activity results in growth defects under stress.** Optical density
1169 (OD_{600}) measurements of *B. fragilis* P207 wild-type (WT) and *cls* single or double mutant strains exposed
1170 to the detergents (**A.**) 0.01% deoxycholate or (**B.**) 0.002% SDS; the salts (**C.**) 300 mM K^+ or (**D.**) 300 mM
1171 Na^+; (**E.**) medium adjusted to pH 5.5; and the ionophores (**F.**) 0.1 µg/mL nigericin or (**G.**) 0.8 µg/mL
1172 monensin A. Untreated (solid lines) and treated cultures (dashed lines) are plotted by strain, with blue,
1173 green and orange/purple indicating *clsA*-, *clsB*- and *clsA clsB*-related strains, respectively. Black indicates
1174 WT. The shaded areas around each line indicate 2× the standard error of the mean of n = 3 biological
1175 replicates.
1176

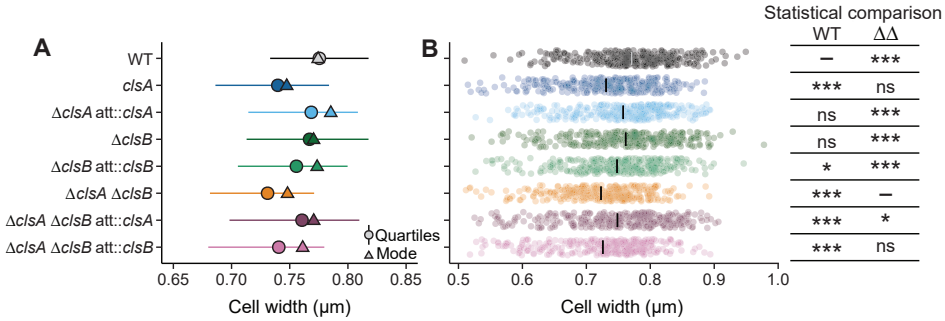

Figure 3. Loss of cardiolipin synthase activity is associated with defects in cell width. A. Summary of the cell width distributions. Horizontal line lengths indicate the 25% and 75% quartiles of the distribution; circles indicate the median; triangles indicates the mode (i.e., the peak of the distribution). **B.** Cell width data for all cells shown in A. plotted by strain (n = 323 cells/strain). The gray or black bars indicate the mean. The table at right shows the results of a mixed-effect linear model comparing strain width to the widths of either WT cells or Δ*clsA* Δ*clsB* double mutant (ΔΔ) cells, as indicated at the top of the column, with a random intercept of biological replicate (i.e., cell width ~ strain + 1|biological replicate). Unadjusted p-values are shown; *, $p < 0.05$, *** $p < 0.001$.

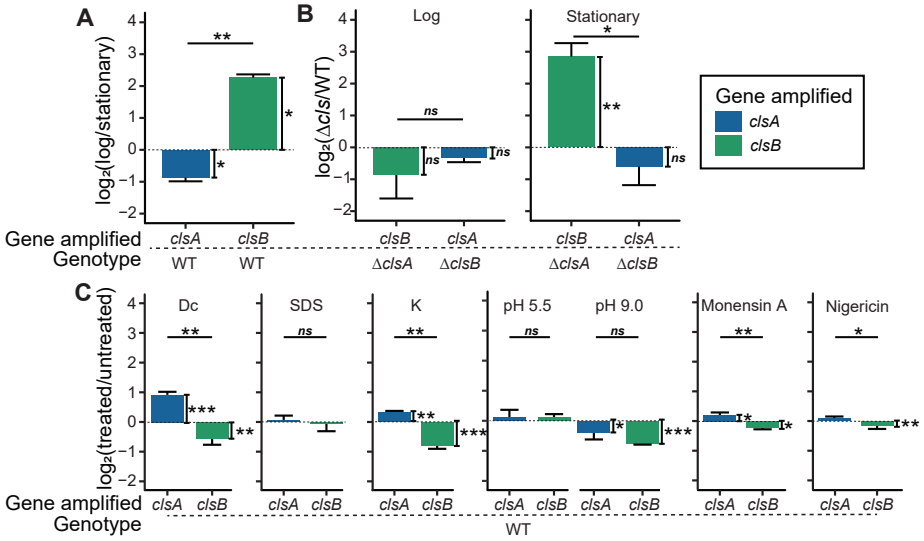

Figure 4. Cardiolipin synthase genes have distinct expression patterns. A. RT-qPCR analysis of relative levels of *clsA* and *clsB* transcripts, shown as the $\log_2$ ratios between log- and stationary-phase growth. **B.** Expression levels of *clsA* or *clsB* when the other gene is knocked out in log- or stationary-phase growth. **C.** *clsA* and *clsB* expression levels in WT *B. fragilis* P207 after 20 min exposure to of 0.01% deoxycholate, 0.002% SDS, 300 mM K, pH 5.5, pH 9.0, 0.8 µg/mL monensin A, or 0.1 µg/mL nigericin. For all panels, values are means ± standard deviation from three biological replicates, each biological replicate value being the mean of three technical replicates. The vertical brackets for statistical analysis assess the significance of the difference between conditions in A and C, between mutant and WT in B. The horizontal brackets for statistical analysis assess the significance of the difference between ΔΔCt values for *clsA* and *clsB* (Students *t*-test). Genes amplified are colored in blue (*clsA*) or green (*clsB*). Error bars indicate standard deviation. Unadjusted p-values are shown; *, $p < 0.05$; **, $p < 0.01$; ***, $p < 0.001$.

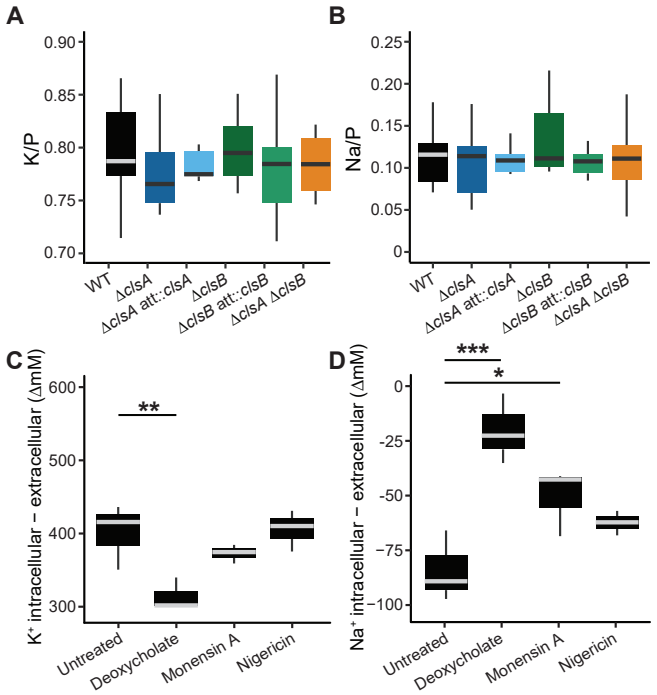

1202

1203 **Figure 5. Stress but not loss of Cls function disrupts membrane ion gradients. A., B.** Abundance of
1204 (**A.**) potassium (K) and (**B.**) sodium (Na) normalized to intracellular phosphorus (P) in *B. fragilis* P207 WT,
1205 Δ*clsA*, Δ*clsB* and complemented strains as well as the Δ*clsA* Δ*clsB* strain, as detected by inductively
1206 coupled plasma mass spectrometry (ICP-MS). **C., D.** Differential concentrations of (**C.**) K^+ and (**D.**) Na^+ in
1207 WT strain cells after a 20 min exposure to 0.01% deoxycholate, 0.8 µg/mL monensin A or 0.1 µg/mL nigericin
1208 (linear regression). The intracellular concentrations (i.e., normalized to cell volume and number of colony-
1209 forming units) with the extracellular concentrations subtracted are shown. For all boxplots, gray or black
1210 lines indicate the median; the top and bottom edges of the box indicate the 25th and 75th percentiles of the
1211 data; the error bars indicate standard deviation (10 biological replicates for untreated conditions and three
1212 for the treatment conditions). Unadjusted p-values are shown; *, $p < 0.05$; **, $p < 0.01$; ***, $p < 0.001$.

1213

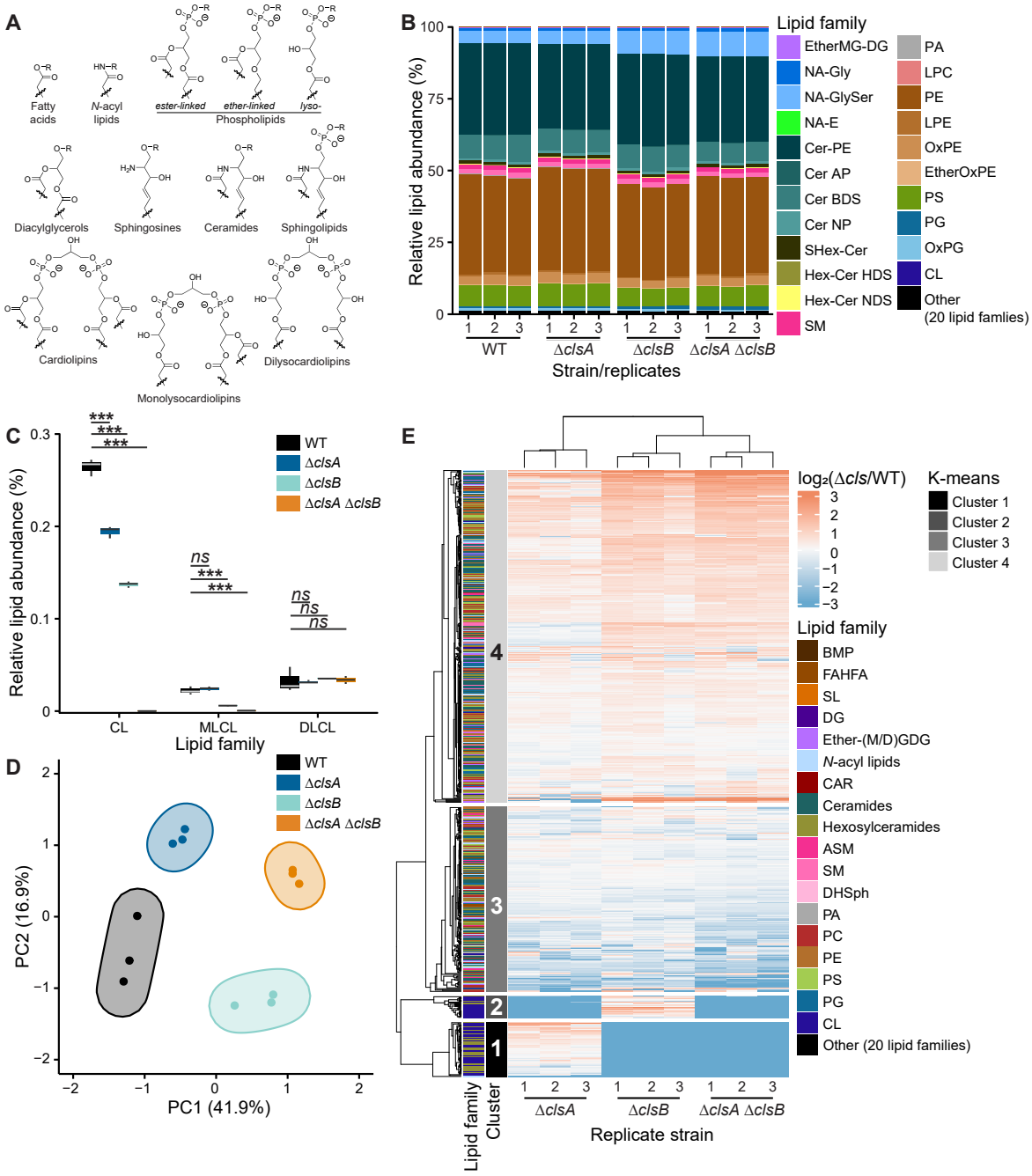

Figure 6. Paralogous cardiolipin synthases produce unique lipid products. A. Structures of lipid families detected by UHPLC-MS/HRMS. For fatty acids, the R-group is H; for saccharolipids, a sugar (i.e., lipid A); and for acyl carnitines, a carnitine. The R-group is H for phosphatidic acid and ethanolamine for phosphatidylethanolamine. Phospholipids are shown as members of three categories: ester-linked (i.e., classical phospholipids), ether-linked and lysophospholipids. Diacylglycerols and monogalactosyl /

1220 monoglucosyl-diacyglycerols have H or a hexose ring as an R-group, respectively. Ceramides, which can
1221 be conjugated to a hexose (i.e., hexosylceramide), are synthesized by *N*-acylating a sphingosine. As
1222 phosphorylated ceramides, sphingolipids have similar R-groups as phospholipids. Length and unsaturation
1223 of the acyl tails are not shown. **B.** Relative abundance of lipid species across WT, Δ*clsA,* Δ*clsB and* Δ*clsA*
1224 Δ*clsB* strains (three biological replicates). Lipid families are abbreviated as follows: PC indicates
1225 phosphatidylcholine; PA, phosphatidic acid; PE, phosphatidylethanolamine; PG, phosphatidylglycerol; PS,
1226 phosphatidylserine; CL, cardiolipin. L-, ML- and DL- indicate lyso-, monolyso- and dilyso-, respectively. **C.**
1227 Relative abundance of cardiolipin, monolyso-cardiolipin and dilysocardiolipin (linear regression).
1228 Unadjusted p-values are shown; ***, $p < 0.001$. **D.** Principal component analysis plot of lipid species in each
1229 strain, with the minimum volume–enclosing ellipses estimated by the Khachiyan algorithm. **E.** Heatmap
1230 representation of the $\log_2$(fold change) of lipid species in each knockout strain compared to WT. Columns
1231 are clustered by similarity and rows by K-means. The left side of the heatmap shows lipid families and K-
1232 means clusters.
1233

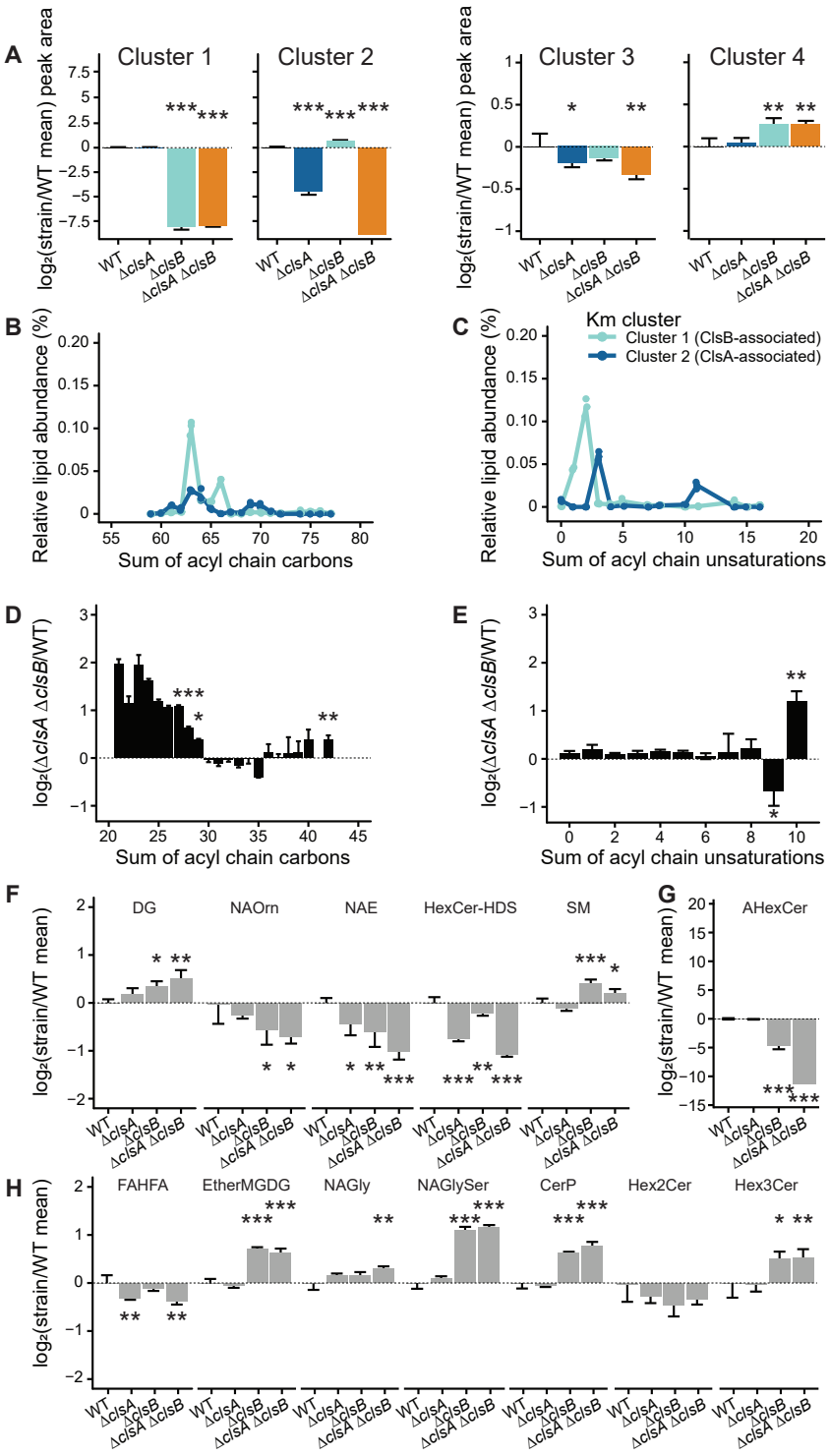

Figure 7. Cardiolipin synthases shape the length and unsaturation level of membrane lipid acyl chains. A. $\log_2$(fold change) of the total peak areas for all lipids in k-means clusters compared to the mean of WT peak areas of that particular cluster (linear regression of peak areas compared to WT). **B., C.** Relative

1238 distribution of sum of acyl chain (**B.**) carbons and (**C.**) unsaturations in cardiolipin and monolysocardiolipin
1239 species of Km clusters 1 (ClsB-associated) and 3 (ClsA-associated) in WT cells. **D., E.** $\log_2$(fold change) of
1240 total two acyl-tailed phospholipids in Δ*clsA* Δ*clsB* strain cells compared to WT shown by (**D.**) acyl chain
1241 length and (**E.**) unsaturations. Student's *t*-test comparing values at designated x-axis values); nd, not
1242 detected (i.e., 0) in the Δ*clsA* Δ*clsB* strain. **F., G., H.** $\log_2$(fold change) of lipids detected in negative (**F.**) and
1243 positive (**G., H.**) ionization mode UHPLC-MS/HRMS comparing each strain to the mean WT peak area.
1244 AHexCer was detected in only 2 and 1 replicates of Δ*clsB* and Δ*clsA* Δ*clsB*, respectively. Lipid families are
1245 abbreviated as follows: DG, diacylglycerol; MG, monogalactosyl/monoglucosyl conjugation; NA, *N*-acyl,
1246 with substituent conjugations indicated for glycyl- (Gly), glycylseryl- (GlySer, ornithine- (Orn), and
1247 ethanolamine- (E); CER, ceramide, with A indicating acyl-, P indicating phospho- and Hex, Hex2 and Hex3
1248 indicating hexosyl-, dihexosyl-, and trihexosyl-; HDS, hydroxy fatty acid-dihydrosphingosine; SM,
1249 sphingomyelin; Ether-, ether-linked (linear regression compared to WT). Across all panels, error bars
1250 indicate standard deviation. Unadjusted p-values are shown; *, $p < 0.05$; **, $p < 0.01$; ***, $p < 0.001$.
1251

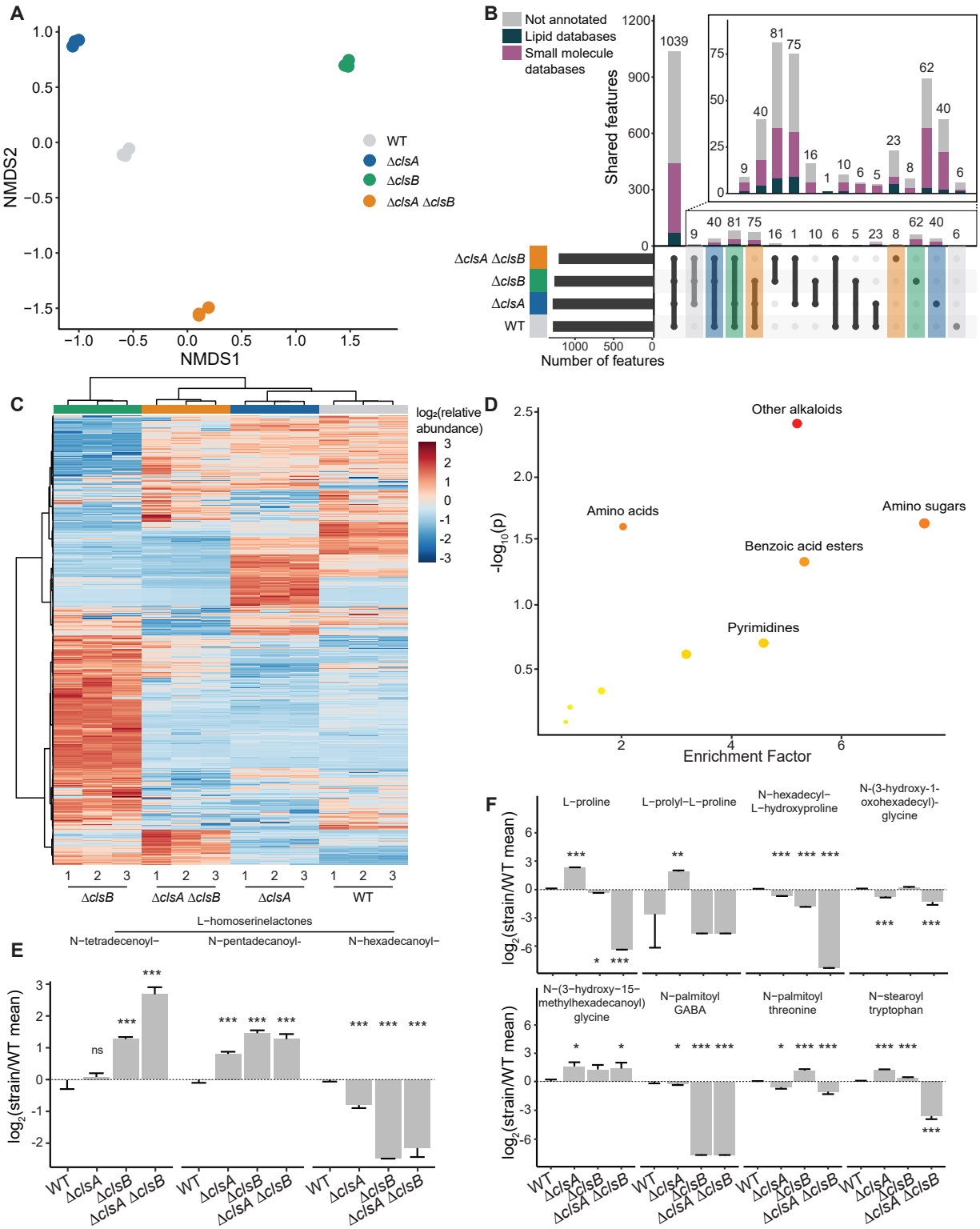

Figure 8. Cardiolipin synthases disrupt metabolic homeostasis. A. NMDS of metabolomics data colored by strain. **B.** Upset plot with the main bar plot color coded for the metabolomic features annotation

1255 sources (dark green = lipid databases, purple = small molecule databases, grey = not annotated within
1256 5ppm error) and the lower section color coded for metabolomic features only present or absent in each
1257 strain (grey = WT, blue = Δ*clsA,* green = Δ*clsB*, orange = Δ*clsA* Δ*clsB*). Inset is a rescaled axis of
1258 metabolites missing in at least one strain. **C.** Heatmap of row normalized abundance of each metabolite in
1259 each strain, clustering by metabolomic features on the vertical axis and samples on the horizontal axis
1260 using Euclidean distance and Ward clustering (3 technical replicates shown for each strain). **D.** Metabolic
1261 pathway analysis with nonlipid sub-categories of *clsAclsB* knockout compared to wildtype (≥3
1262 features/pathway). The x-axis represents the enrichment factor computed from pathway topological
1263 analysis on non-lipid species, and the y-axis is the log of p-value obtained from pathway enrichment
1264 analysis. The pathways that were most significantly changed are characterized by both a high-log(p) value
1265 and high enrichment factor (top right region). **E., F.** Abundance of compounds in enriched pathways for (E)
1266 lipid-conjugated homoserine lactones and (F) fatty amides (top enriched pathways) (mean and standard
1267 deviation of 3 technical replicates shown; linear regression compared to WT). Across all panels, error bars
1268 indicate standard deviation. Unadjusted p-values are shown; *, $p < 0.05$; **, $p < 0.01$; ***, $p < 0.001$.
1269

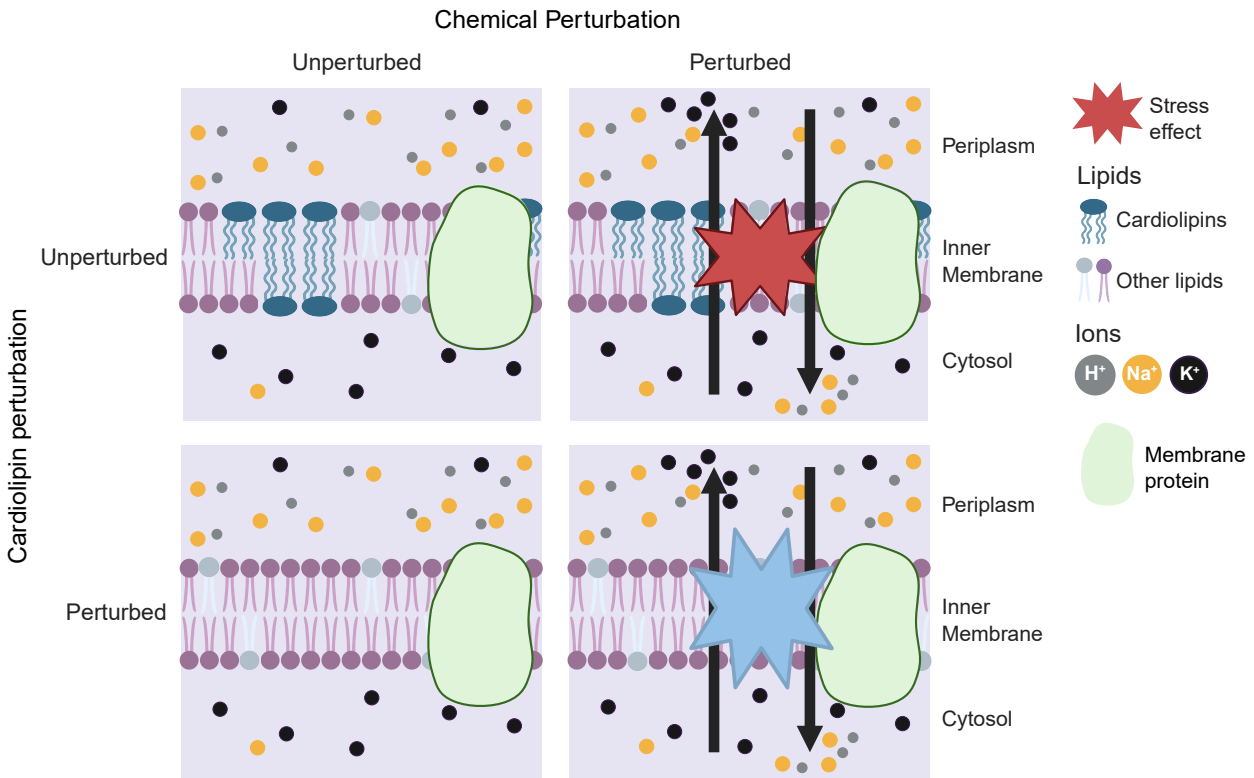

Figure 9. Cardiolipins mitigate the fitness cost of membrane stress in *B. fragilis*. In unperturbed cells, ion gradients are maintained across the inner membrane, with higher extracellular concentrations of H^+ and Na^+ and elevated intracellular K^+ (top left). The outer membrane is generally permeable to these ions due to the presence of porins. In the absence of cardiolipin, *B. fragilis* remodels its membrane lipid composition, which presumably helps to maintain ion gradients (bottom left). Chemical membrane (or membrane ion gradient) perturbation alters *cls* gene expression and ion homeostasis (top right). In the absence of cardiolipins, cells are more susceptible to chemical membrane perturbations (bottom right). The larger blue star indicates the greater fitness cost associated with membrane perturbation in cardiolipin-deficient cells, particularly *clsB* mutants. In contrast, the smaller red star reflects reduced stress susceptibility in cells that retain cardiolipin synthesis.

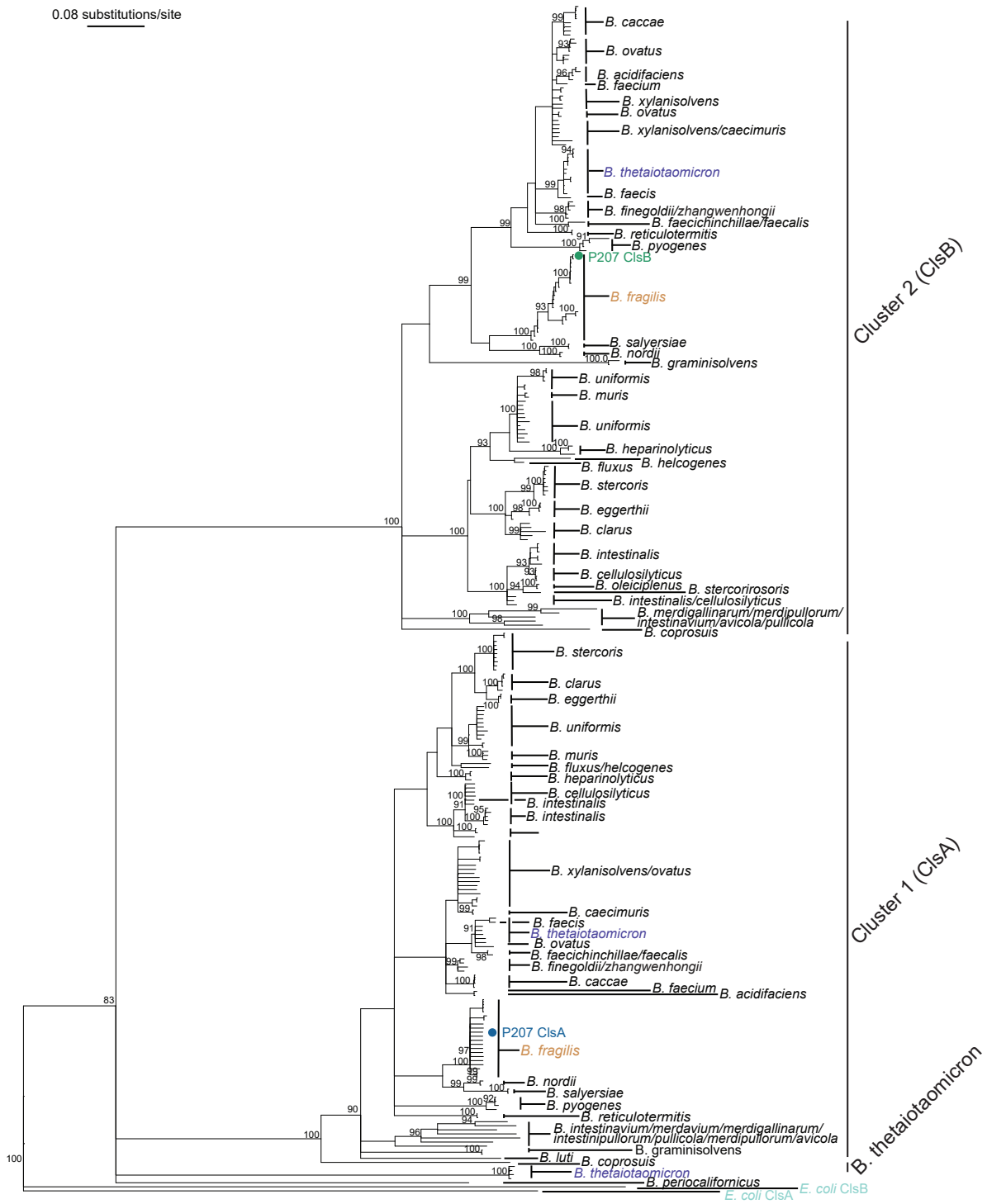

Figure S1. Neighbor-joining tree of cardiolipin synthases from *Bacteroides* species. Clusters 1 (ClsA), 2 (ClsB) and 3 (not named) of *Bacteroides* Cls proteins are indicated. *E. coli* ClsA was designated as an outgroup. ClsA and ClsB of *B. fragilis* P207 are colored in blue and green, respectively. Other strains

1285 of *B. fragilis, B. thetaiotaomicron*, and *E. coli* are colored in gold, purple and light blue, respectively. Taxa
1286 labels with similar tree positions are combined for clarity at times (i.e., *B. xylanisolvens/caecimuris*). Key
1287 indicates the rate of amino acid substitutions per site. Bootstrap values are generally shown only if ≥90.
1288

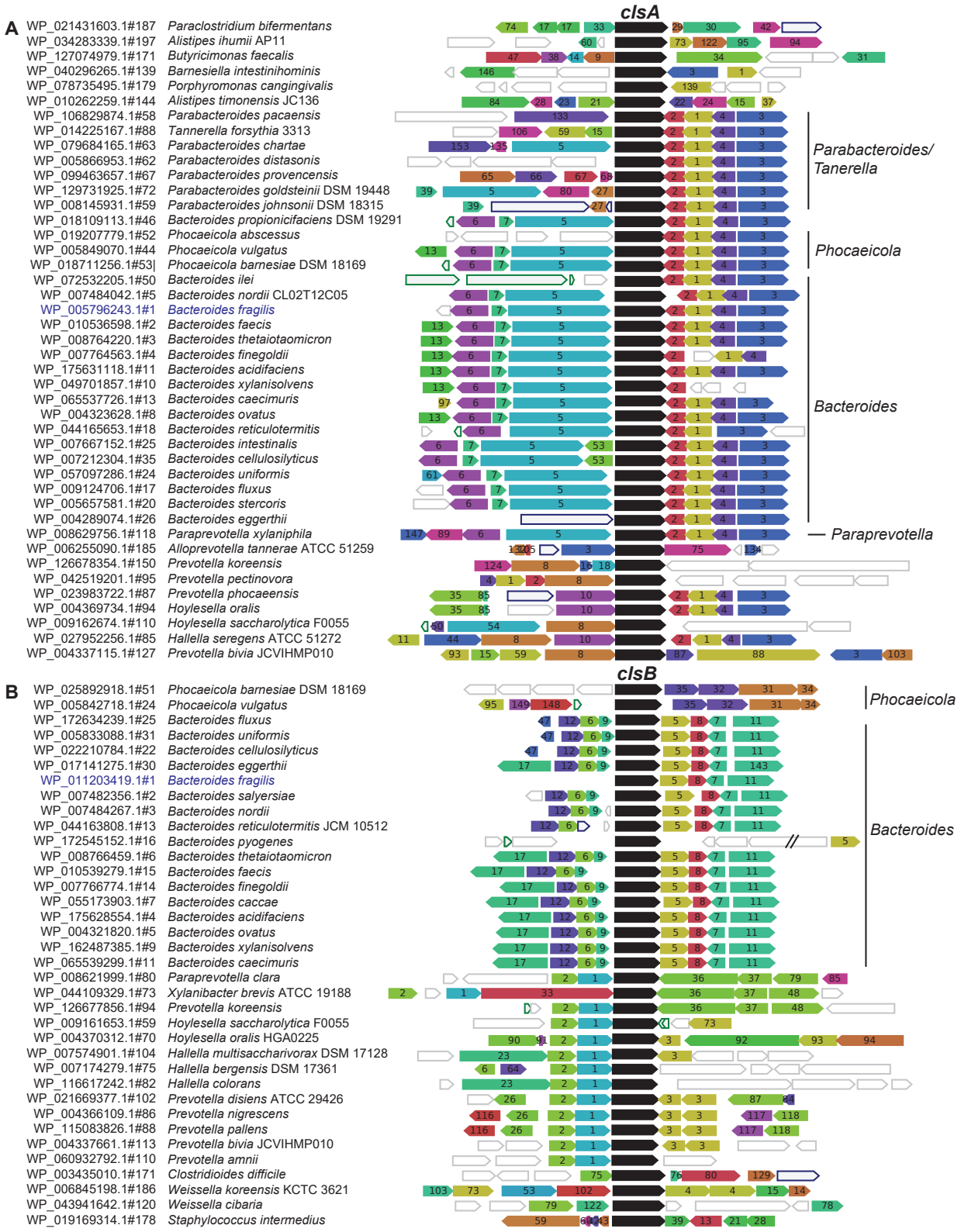
A
clsA
WP_021431603.1#187 Paraclostridium bifermentans
WP_034283339.1#197 Alistipes ihumii AP11
WP_127074979.1#171 Butyricimonas faecalis
WP_040296265.1#139 Barnesiella intestinihominis
WP_078735495.1#179 Porphyromonas cangingivalis
WP_010262259.1#144 Alistipes timonensis JC136
WP_106829874.1#58 Parabacteroides pacaensis
WP_014225167.1#88 Tannerella forsythia 3313
WP_079684165.1#63 Parabacteroides chartae
WP_005866953.1#62 Parabacteroides distasonis
WP_099463657.1#67 Parabacteroides provencensis
WP_129731925.1#72 Parabacteroides goldsteinii DSM 19448
WP_008145931.1#59 Parabacteroides johnsonii DSM 18315
WP_018109113.1#46 Bacteroides propionicifaciens DSM 19291
WP_019207779.1#52 Phocaeicola abscessus
WP_005849070.1#44 Phocaeicola vulgatus
WP_018711256.1#53| Phocaeicola barnesiae DSM 18169
WP_072532205.1#50 Bacteroides ilei
WP_007484042.1#5 Bacteroides nordii CL02T12C05
WP_005796243.1#1 Bacteroides fragilis
WP_010536598.1#2 Bacteroides faecis
WP_008764220.1#3 Bacteroides thetaiotaomicron
WP_007764563.1#4 Bacteroides finegoldii
WP_175631118.1#11 Bacteroides acidifaciens
WP_049701857.1#10 Bacteroides xylanisolvens
WP_065537726.1#13 Bacteroides caecimuris
WP_004323628.1#8 Bacteroides ovatus
WP_044165653.1#18 Bacteroides reticulotermitis
WP_007667152.1#25 Bacteroides intestinalis
WP_007212304.1#35 Bacteroides cellulosilyticus
WP_057097286.1#24 Bacteroides uniformis
WP_009124706.1#17 Bacteroides fluxus
WP_005657581.1#20 Bacteroides stercoris
WP_004289074.1#26 Bacteroides eggerthii
WP_008629756.1#118 Paraprevotella xylaniphila
WP_006255090.1#185 Alloprevotella tannerae ATCC 51259
WP_126678354.1#150 Prevotella koreensis
WP_042519201.1#95 Prevotella pectinovora
WP_023983722.1#87 Prevotella phocaeensis
WP_004369734.1#94 Hoylesella oralis
WP_009162674.1#110 Hoylesella saccharolytica F0055
WP_027952256.1#85 Hallella seregens ATCC 51272
WP_004337115.1#127 Prevotella bivia JCVIHMP010
Parabacteroides/ Tanerella
Phocaeicola
Bacteroides
Paraprevotella
B
clsB
WP_025892918.1#51 Phocaeicola barnesiae DSM 18169
WP_005842718.1#24 Phocaeicola vulgatus
WP_172634239.1#25 Bacteroides fluxus
WP_005833088.1#31 Bacteroides uniformis
WP_022210784.1#22 Bacteroides cellulosilyticus
WP_017141275.1#30 Bacteroides eggerthii
WP_011203419.1#1 Bacteroides fragilis
WP_007482356.1#2 Bacteroides salyersiae
WP_007484267.1#3 Bacteroides nordii
WP_044163808.1#13 Bacteroides reticulotermitis JCM 10512
WP_172545152.1#16 Bacteroides pyogenes
WP_008766459.1#6 Bacteroides thetaiotaomicron
WP_010539279.1#15 Bacteroides faecis
WP_007766774.1#14 Bacteroides finegoldii
WP_055173903.1#7 Bacteroides caccae
WP_175628554.1#4 Bacteroides acidifaciens
WP_004321820.1#5 Bacteroides ovatus
WP_162487385.1#9 Bacteroides xylanisolvens
WP_065539299.1#11 Bacteroides caecimuris
WP_008621999.1#80 Paraprevotella clara
WP_044109329.1#73 Xylanibacter brevis ATCC 19188
WP_126677856.1#94 Prevotella koreensis
WP_009161653.1#59 Hoylesella saccharolytica F0055
WP_004370312.1#70 Hoylesella oralis HGA0225
WP_007574901.1#104 Hallella multisaccharivorax DSM 17128
WP_007174279.1#75 Hallella bergensis DSM 17361
WP_116617242.1#82 Hallella colorans
WP_021669377.1#102 Prevotella disiens ATCC 29426
WP_004366109.1#86 Prevotella nigrescens
WP_115083826.1#88 Prevotella pallens
WP_004337661.1#113 Prevotella bivia JCVIHMP010
WP_060932792.1#110 Prevotella amnii
WP_003435010.1#171 Clostridioides difficile
WP_006845198.1#186 Weissella koreensis KCTC 3621
WP_043941642.1#120 Weissella cibaria
WP_019169314.1#178 Staphylococcus intermedius
Phocaeicola
Bacteroides

1289

1290 **Figure S2. Genomic neighborhood synteny indicates the ancestral introduction of *clsA* and *clsB***
1291 **into the *Bacteroides.*** Curated WebFlags2 output of (**A.**) *clsA* and (**B.**) *clsB* genomic neighborhoods. *B.*
1292 *fragilis* is colored blue. Genera of interest with similar levels of gene conservation are indicated at right.
1293

1294

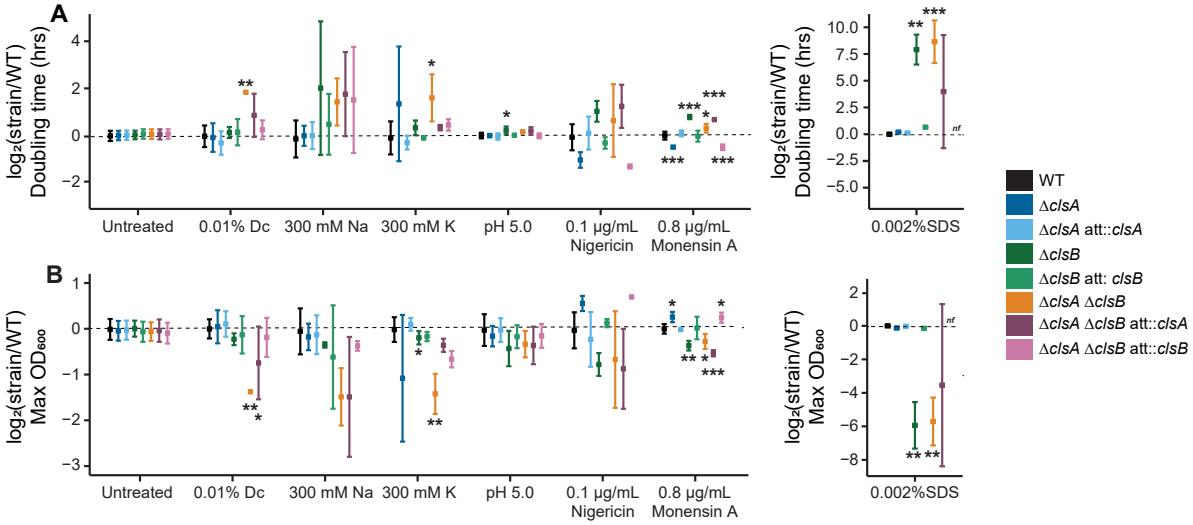

1295

1296 **Figure S3. Loss of cardiolipin synthase activity results in growth defects under stress. A., B.** $\log_2$(fold
1297 change) of (**A.**) doubling time and (**B.**) maximum OD_{600} comparing *B. fragilis* wild-type (WT) and *cls* mutants
1298 to the average of WT in that condition. Metrics were calculated from 24-h growth curves in BHIS medium
1299 alone or containing 0.01% deoxycholate (Dc), 0.002% sodium dodecyl sulfate (SDS), 300 mM sodium
1300 (Na^+), 300 mM potassium (K^+), and 0.01 µg/mL nigericin and 0.8 µg/mL monensin A. Any doubling time
1301 ≥100 h was considered as no growth. The dashed horizontal line indicates no change from the average of
1302 WT. Strain are colored with blue (*clsA-related*), green (*clsB*-related) and orange/purple (*clsA clsB*-related).
1303 Black indicates WT. The vertical lines indicate mean; the ends of the whiskers ± standard deviation (linear
1304 regression compared to WT). Three biological replicates for each condition were run, each run in technical
1305 triplicate. nf, no accurate fit of growth data by the polynomial was found. Unadjusted p-values are shown;
1306 *, $p < 0.05$; **, $p < 0.01$; ***, $p < 0.001$.

1307

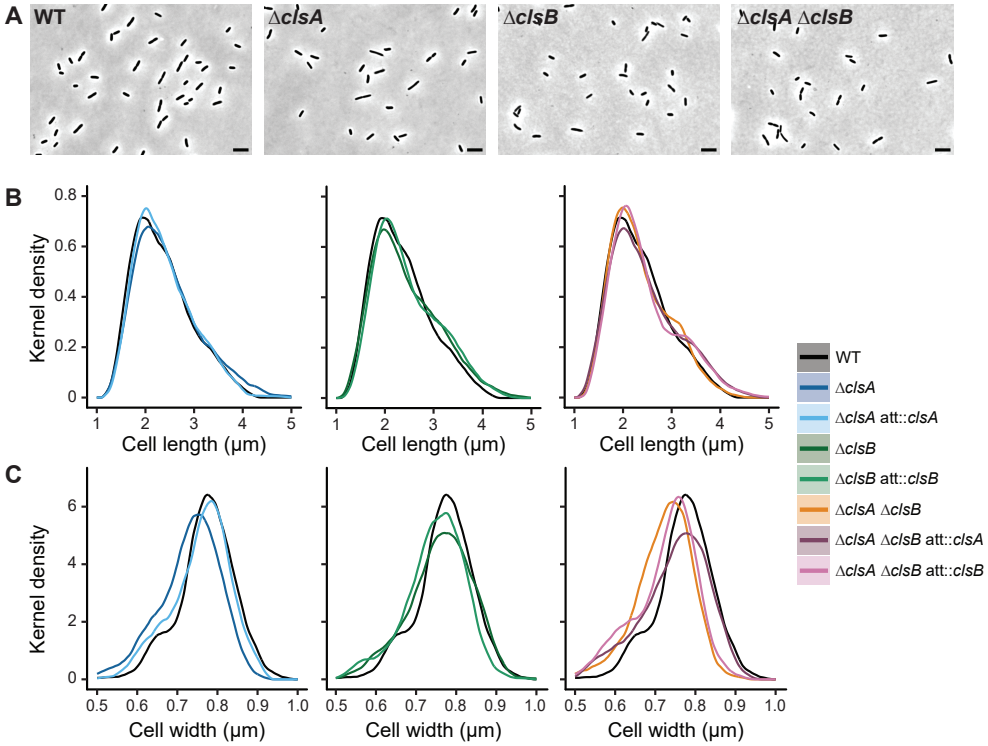

1308

1309 **Figure S4. Loss of cardiolipin synthase activity is associated with defects in cell width. A.** Phase-

1310 contrast microscopy images of *B. fragilis* P207 WT, Δ*clsA*, Δ*clsB* and Δ*clsA* Δ*clsB* strains. Scale bars, 5 μm.

1311 **B., C.** Distributions estimated by kernel density of (**B.**) cell length and (**C.**) cell width. Results are plotted by

1312 strain with blue, green and orange/purple indicating *clsA*-, *clsB*- and *clsA clsB*-related strains, respectively.

1313 Black indicates WT.

1314

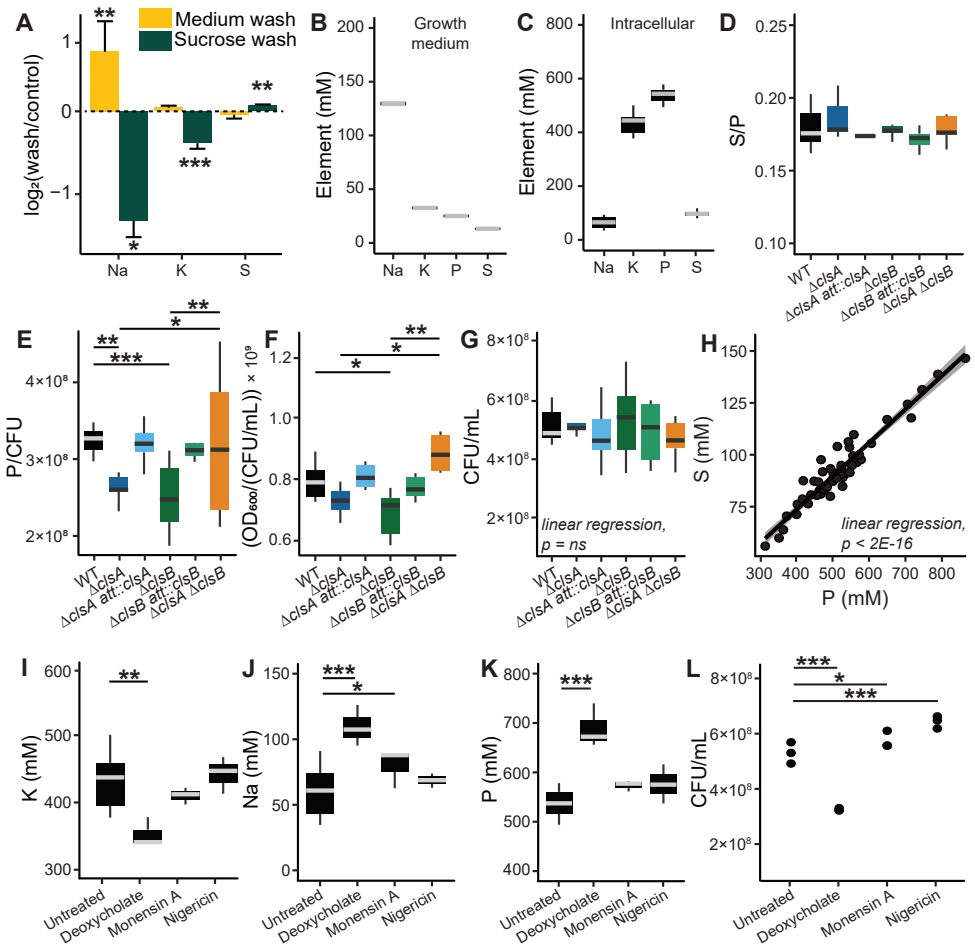

Figure S5. Washing but not loss of *cls* genes disrupts intracellular elemental concentrations. Inductively coupled plasma mass spectrometry (ICP-MS) analysis using wash-free sample preparation to quantify intracellular elemental concentrations. **A.** $\log_2$(fold change) of elements comparing unwashed cells to cell pellets washed with either BHIS growth medium or an isotonic sucrose solution. Error bars indicate standard deviation. **B.** Concentrations of detected elements in BHIS growth medium. **C.** Intracellular concentrations of detected elements in WT *B. fragilis* P207. **D.** Intracellular sulfur in *B. fragilis* P207 strains normalized to P. **E.** Intracellular phosphorus (P) per 10^6 colony-forming units (CFU) in *B. fragilis* P207 wild-type (WT), Δ*clsA*, Δ*clsB* and Δ*clsA* Δ*clsB* strains. **F.** OD_{600} normalized to CFU per mL of strain cultures used in ICP-MS input. **G.** Raw CFU/mL of each strain shown in panels F and G. **H.** Intracellular P content compared to sulfur (S) content across *cls* strains and treatment conditions. **I., J.** Intracellular concentrations of (**I.**) K^+ and (**J.**) Na^+ after a 20 min exposure to 0.01% deoxycholate, 0.8 µg/mL monensin A and 0.1 µg/mL nigericin. Each treatment had the same culture input. **K.** Intracellular P concentrations of *B. fragilis* WT cells

1328 after 20 min of exposure to the indicated stress conditions. **L.** CFU/mL of strain cultures after exposure to
1329 the treatments in **I–L**. For all boxplots, the gray or black middle lines indicate the median; the top and
1330 bottom edges of the box indicate the 25th and 75th percentiles of n = 3 replicates for wash and treatment
1331 experiments and n = 10 replicates for rest. Whiskers indicate 1.5× the interquartile range (IQR). For the
1332 linear regression, the shade ribbon indicates standard error of the mean. All statistical comparisons were
1333 made using linear regression, with unadjusted p-values shown; *, $p < 0.05$; **, $p < 0.01$; ***, $p < 0.001$.
1334

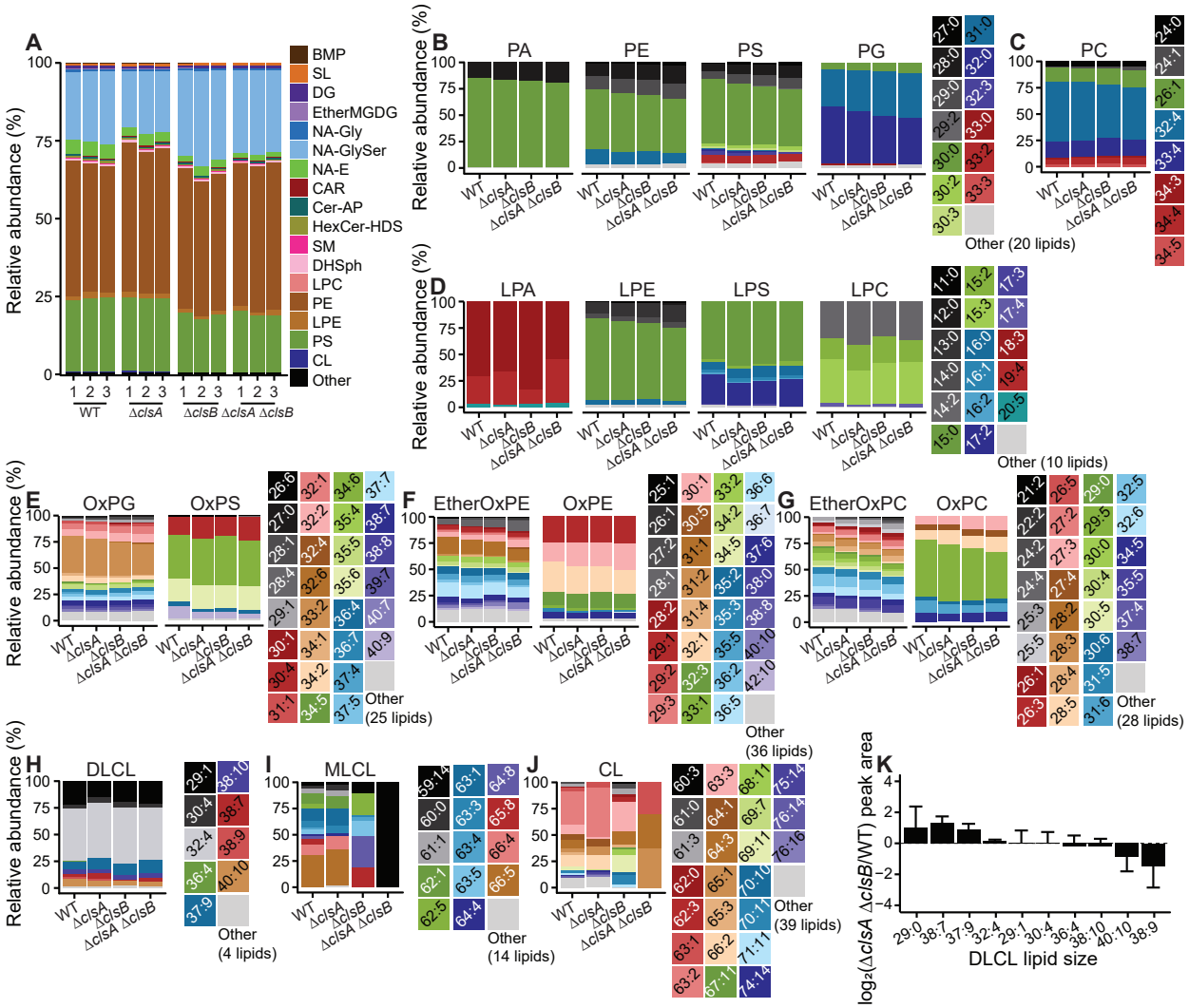

Figure S6. Cardiolipin synthases shape the membrane lipid population. A-J. Relative abundance of lipid species in membranes across *B. fragilis* WT, Δ*clsA*, Δ*clsB*, and Δ*clsA* Δ*clsB* strains in positive (**A.**) or negative (**B-J.**) electrospray ionization modes for UHPLC–MS/HRMS. For **A,** colors designate lipid family. Positive-mode lipid families are abbreviated as follows: BMP, bismonoacylglycerophosphate; SL, saccharolipids; DG, diacylglycerol; EtherMG, ether-linked with monogalactosyl/monoglucosyl conjugation; NA, *N*-acyl, with substituent conjugations indicated for glycyl- (Gly), glycylserine- (GlySer), and ethanolamine- (E); CAR, acylcarnitine; CER, ceramide, AP indicating alpha-hydroxy fatty acid-phytospingosine and Hex indicating hexosyl-; SM, sphingomyelin; DHSph, sphinganine (please see the legend for panel E for other abbreviations). For **B-J**, species are colored based on the total number of

1346 carbons in their acyl chains. Lipids at <1% abundance are colored gray, with the number of lipid species in
1347 this category indicated in the figure. Relative abundance plots are grouped as (**B.**) two or (**C.**) one acyl-
1348 tailed phospholipid species, with oxidized and ether-linked lipids shown in **E.-G.**, or (**H.**) dilysocardiolipin,
1349 (**I.**) monolysocardiolipin or (**J.**) cardiolipin species. Negative-mode lipid families are abbreviated as follows:
1350 PA, phosphatidic acid; PE, phosphatidylethanolamine; PS, phosphatidylserine; PG, phosphatidylglycerol;
1351 PC, phosphatidylcholine; CL, cardiolipin. L-, ML- and DL- indicate lyso-, monolyso- and dilyso-, respectively.
1352 Ox and Ether indicate oxidized and ether-linked, respectively. **K.** $\log_2$(fold change) peak area of
1353 dilysocardiolipin species comparing Δ*clsA* Δ*clsB* to WT (linear regression, $p < 0.00029$; $\log_{10}$[peak area] ~
1354 strain + DLCL species). Error bars indicate standard deviation.
1355

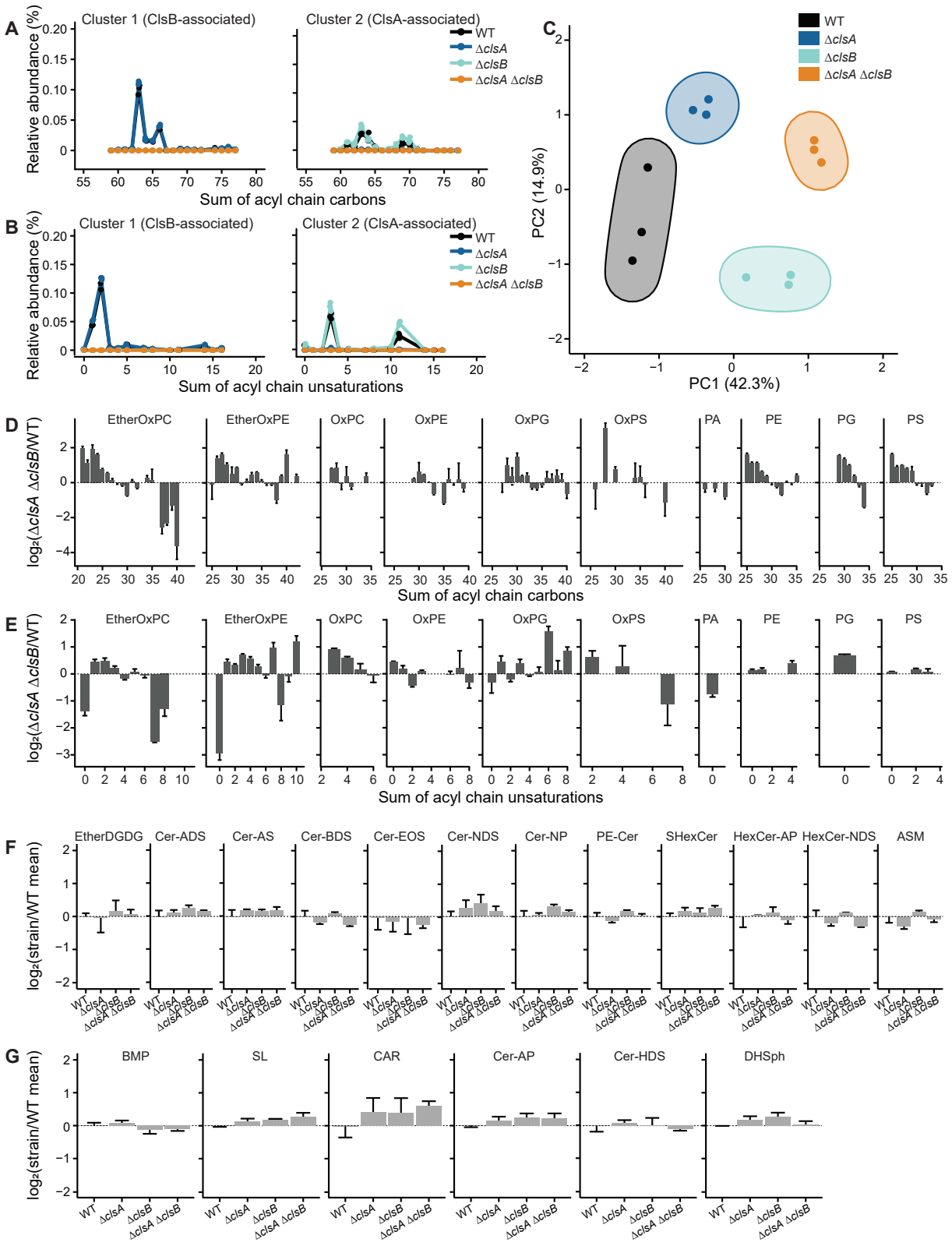
A
Cluster 1 (ClsB-associated)
Cluster 2 (ClsA-associated)
Relative abundance (%)
Sum of acyl chain carbons
WT
ΔclsA
ΔclsB
ΔclsA ΔclsB
B
Sum of acyl chain unsaturations
C
PC1 (42.3%)
PC2 (14.9%)
D
log2(ΔclsA ΔclsB/WT)
EtherOxPC
EtherOxPE
OxPC
OxPE
OxPG
OxPS
PA
PE
PG
PS
E
F
log2(strain/WT mean)
EtherDGDG
Cer-ADS
Cer-AS
Cer-BDS
Cer-EOS
Cer-NDS
Cer-NP
PE-Cer
SHexCer
HexCer-AP
HexCer-NDS
ASM
G
BMP
SL
CAR
Cer-AP
Cer-HDS
DHSph

1358 **Figure S7. Cardiolipin synthases produce unique lipid products and their loss remodels overall**
1359 **membrane lipid composition. A., B.** Relative abundance of lipids from K-means clusters 1 and 2 across
1360 *B. fragilis* WT, Δ*clsA*, Δ*clsB* and Δ*clsA* Δ*clsB* strains plotted by (**A.**) acyl chain length or (**B.**) acyl chain
1361 unsaturations. **C.** Principal component analysis plot of lipids in the *B. fragilis* membrane excluding
1362 cardiolipin and monolysocardiolipin species. Minimum volume-enclosing ellipses were estimated using
1363 the Khachiyan algorithm. **D., E.** $\log_2$(fold change) of Pa, PE, PG and PS lipids in Δ*clsA* Δ*clsB* cells
1364 compared to WT plotted by the sum of acyl chain (**D.**) carbons or (**E.**) unsaturations. **F., G.** $\log_2$(fold
1365 change) of lipids detected in (**F.**) negative or (**G.**) positive ionization modes with values for each strain
1366 compared to the mean abundance in WT cells. See figures 7 and S6 for lipid family abbreviations. Error
1367 bars indicate standard deviation. Unadjusted p-values are shown.

1368

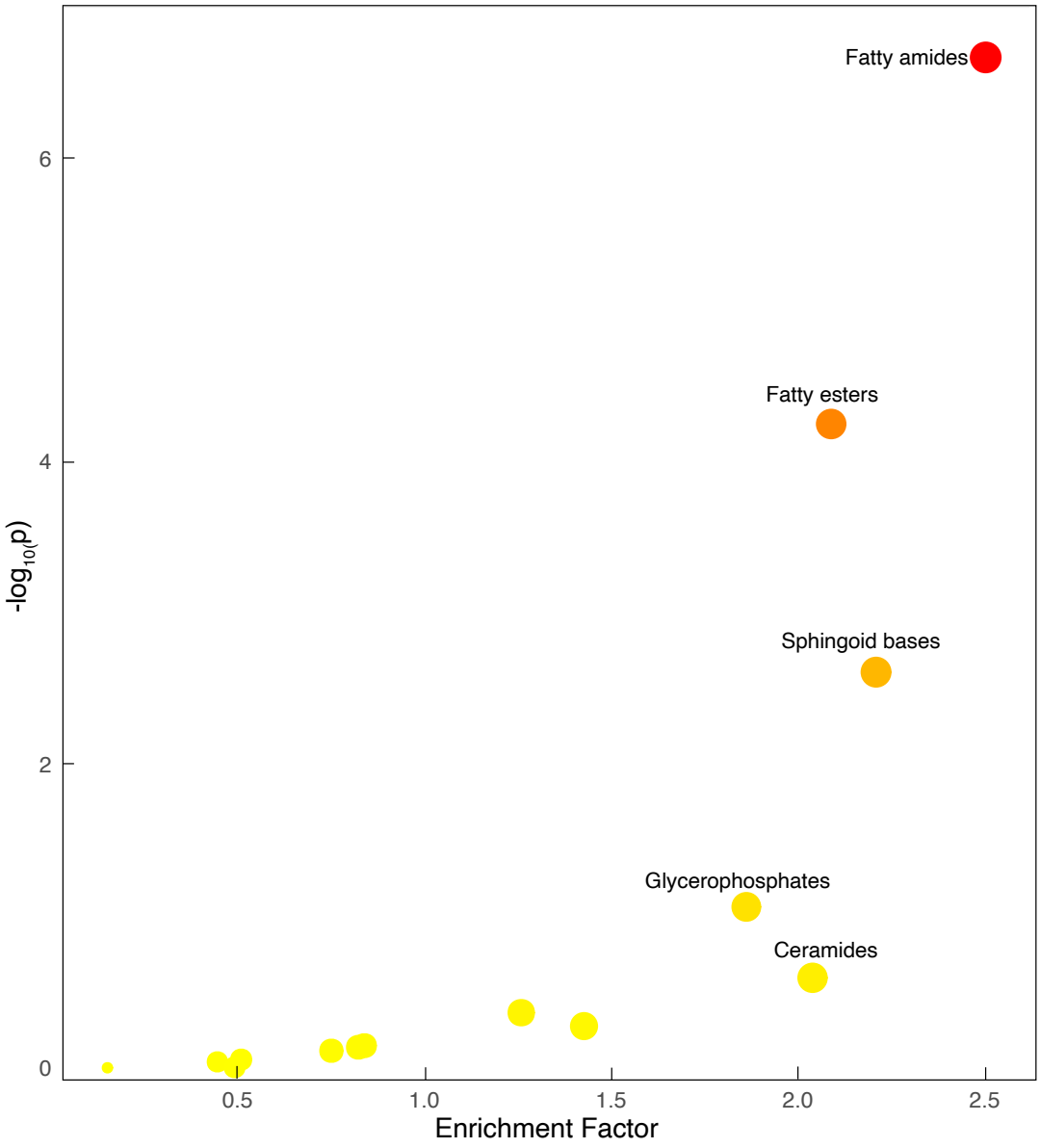

Figure S8. Pathway enrichment analysis for main lipid categories. Pathway analysis is performed with MetaboAnalyst 6.0, with default mummichog parameters with p-value cutoff of 0.0005 and lipid – main chemical class as the selected metabolite sets containing at least 3 entries.

1374

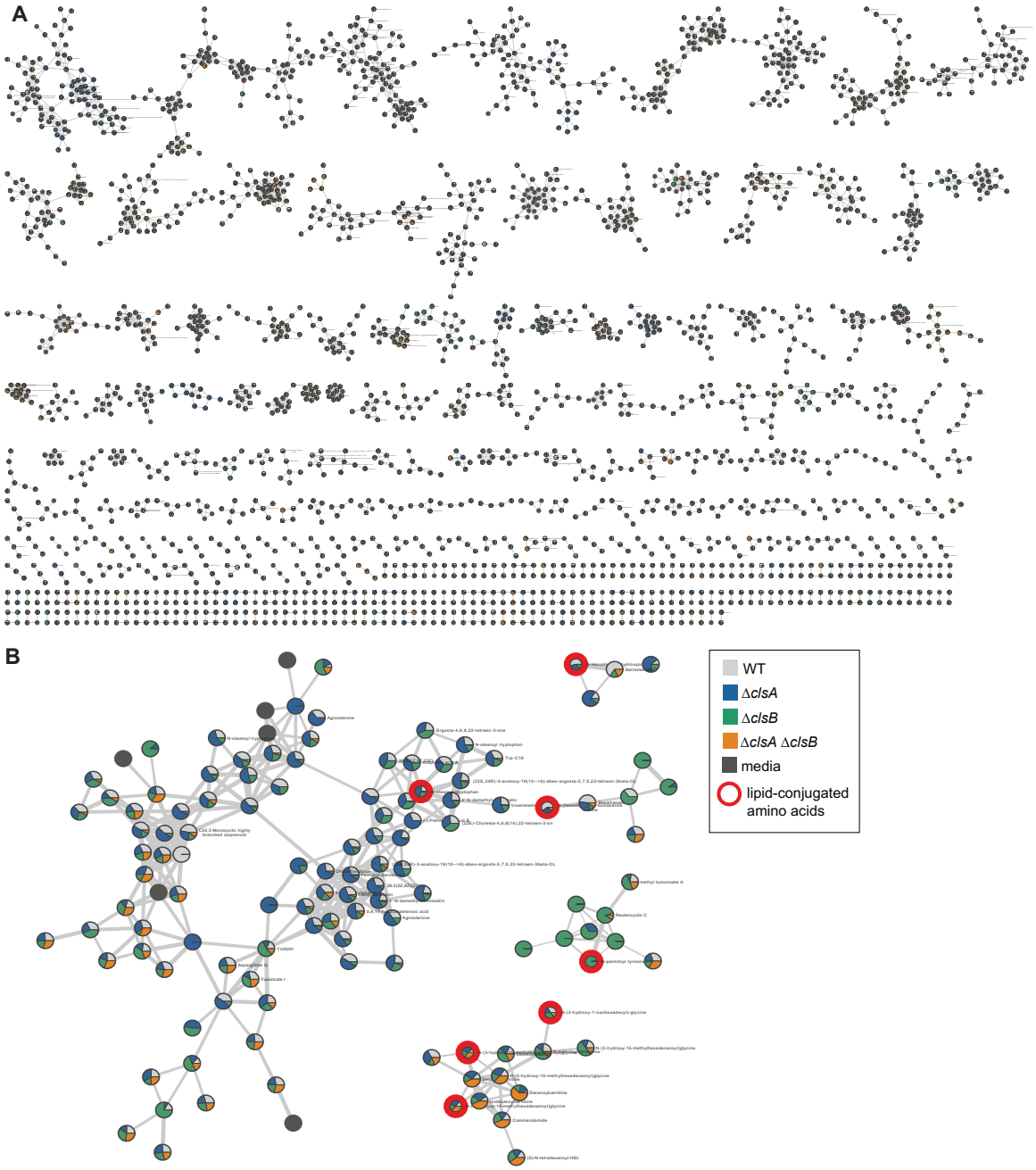

1375

1376 **Figure S9. Molecular networking shows chemically related metabolites in *B. fragilis* strains. A.**

1377 Feature-based molecular networking of all features (excluding singletons) from WT, Δ*clsA*, Δ*clsB*, Δ*clsA*

1378 Δ*clsB*, and extracted BHIS media. Each feature is a node, connected by an edge calculated from cosine

similarity score. **B.** Subset of features connected by an edge to fatty amides highlighted in Fig. 8 (red border). Each pie chart in the node is colored by relative abundance of the feature in each strain.

Table S1. Primers and vectors used in this study.

Table S2. Strains used in this study.

Table S3. Metadata for genomics analyses.

Table S4. Raw data for the lipidomics analyses.

Table S5. Raw data for the ICP-MS analyses.

Table S6. Raw data for untargeted metabolomics analyses.

Table S7. Pathway enrichment analysis for main lipid categories.

Table S8. Pathway enrichment analysis for sub non-lipid categories.